

## Ferrielectricity in $\text{DyMn}_2\text{O}_5$ : A golden touchstone for multiferroicity of $\text{RMn}_2\text{O}_5$ family\*

J.-M. Liu<sup>†,§</sup> and S. Dong<sup>‡</sup>

<sup>†</sup>Laboratory of Solid State Microstructures  
 and Innovation Center of Advanced Microstructures  
 Nanjing University, Nanjing 210093, P. R. China

<sup>‡</sup>Department of Physics, Southeast University, Nanjing 211189, P. R. China  
<sup>§</sup>liujm@nju.edu.cn

Received 17 May 2015; Accepted 2 June 2015; Published 23 June 2015

The  $\text{RMn}_2\text{O}_5$  manganite compounds represent one class of multiferroic family with magnetic origins, which has been receiving continuous attention in the past decade. So far, our understanding of the magnetic origins for ferroelectricity in  $\text{RMn}_2\text{O}_5$  is associated with the nearly collinear antiferromagnetic structure of Mn ions, while the exchange striction induced ionic displacements are the consequence of the spin frustration competitions. While this scenario may be applied to almost all  $\text{RMn}_2\text{O}_5$  members, its limitation is either clear: the temperature-dependent behaviors of electric polarization and its responses to external stimuli are seriously materials dependent. These inconsistencies raise substantial concern with the state-of-the-art physics of ferroelectricity in  $\text{RMn}_2\text{O}_5$ . In this mini-review, we present our recent experimental results on the roles of the  $4f$  moments from R ions which are intimately coupled with the  $3d$  moments from Mn ions.  $\text{DyMn}_2\text{O}_5$  is a golden figure for illustrating these roles. It is demonstrated that the spin structure accommodates two nearly collinear sublattices which generate respectively two ferroelectric (FE) sublattices, enabling  $\text{DyMn}_2\text{O}_5$  an emergent ferrielectric (FIE) system rarely identified in magnetically induced FEs. The evidence is presented from several aspects, including FIE-like phenomena and magnetoelectric responses, proposed structural model, and experimental check by nonmagnetic substitutions of the  $3d$  and  $4f$  moments. Additional perspectives regarding possible challenges in understanding the multiferroicity of  $\text{RMn}_2\text{O}_5$  as a generalized scenario are discussed.

**Keywords:**  $\text{RMn}_2\text{O}_5$ ; multiferroic; ferrielectricity;  $3d$ - $4f$  coupling; exchange striction.

### 1. Introduction

Multiferroic compounds of magnetically induced ferroelectricity, as promising magnetoelectric materials for immediate applications, are more or less despised currently but have been receiving continuous attention from the condensed matter physics community.<sup>1–4</sup> On one hand, these compounds do enable a generation of ferroelectricity by magnetism-relevant mechanisms rather than lattice phonon-mode softening widely known in textbooks of ferroelectricity,<sup>5–7</sup> since such phenomena had never been observed in realistic materials before. On the other hand, the strong coupling between electric polarization ( $P$ ) and magnetization ( $M$ ) plus their cross-controls via electric and magnetic stimuli routes have inspired continuous interest in the underlying mechanisms.<sup>8–11</sup> It is believed that these mechanisms for ferroelectricity generation and magnetoelectric cross-controls may be useful in searching for novel multiferroics with improved performances at high temperatures ( $T$ ).<sup>12,13</sup>

Up to date, extensive investigations on these emergent phenomena show off two major microscopic mechanisms for ferroelectricity generation,<sup>8,11,14</sup> as sketched in Figs. 1(a)

and 1(b) for a guide of eyes where a charge-ordered spin chain is chosen for illustration, although other mechanisms for individuals were proposed.<sup>15–17</sup> Details for discovering these phenomena and relevant physics can be found in several recent review papers.<sup>1,3</sup> Figure 1(a) shows a noncollinear spin chain where a spin-pair is bridged by a ligand ion (e.g., oxygen O) and the spins are noncollinearly ordered in counterclockwise spiral (a1) or clockwise spiral (a2) alignment.<sup>18</sup> The relativistic correction of the spin–orbit coupling to the exchange interaction, i.e., the so-called Dzyaloshinskii–Moriya interaction (DMI), drives a small shift of the ligand ions, since the exchange interaction can be enhanced at the cost of the shift-induced lattice energy.<sup>8,9,14</sup> Given the spiral spin order along the chain direction, all the ligand ions shift along the same direction, leading to a net electric polarization perpendicular to the spin chain. This is the DMI mechanism and the generated polarization  $P(\Delta P) \sim e_{ij} \times (S_i \times S_j)$ . The other mechanism refers to some specific collinear spin orders and one example is illustrated in Fig. 1(b) where the spin chain favors the  $\uparrow\uparrow\downarrow\downarrow$  collinear order.<sup>11,19</sup> The symmetric exchange striction drives the two parallel nearest spins to near

\*In celebration of the eightieth birthday of Prof. Xi Yao.

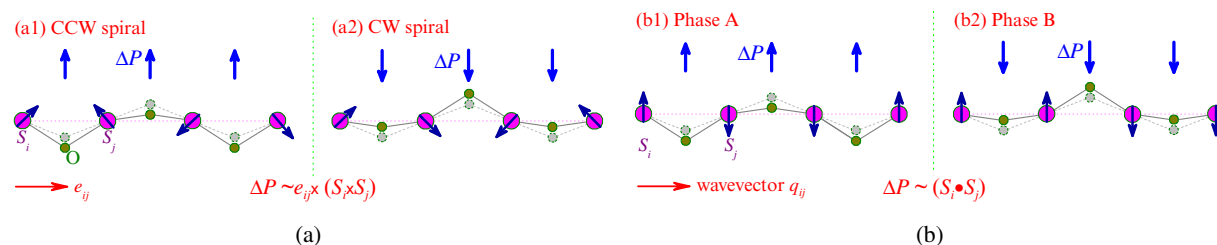


Fig. 1. (Color online) Two major microscopic mechanisms for polarization generations in single phase multiferroic compounds.<sup>18</sup> (a) The Dzyaloshinskii–Moriya interaction (DMI) mechanism associated with a noncollinear spiral spin order and the local polarization  $P(\Delta P) \sim e_{ij} \times (S_i \times S_j)$  where  $e_{ij}$  is a vector connecting one neighboring spin pair  $S_i$  and  $S_j$  bridged with oxygen as a ligand. (b) The symmetric exchange striction mechanism associated with a collinear  $\uparrow\uparrow\downarrow\downarrow$  (or  $\leftarrow\leftarrow\rightarrow\rightarrow$ ) spin order and the local  $P(\Delta P)$  is proportional to  $S_i \cdot S_j$  where the spin pair  $S_i$  and  $S_j$  is bridged with oxygen as a ligand.

with each other and those antiparallel to apart from each other. Concomitantly, the ligand ions bridging the spin pairs will shift towards and away from the chain, respectively, leading to net polarizations  $P(\Delta P) \sim (S_i \cdot S_j)$ . It is called the exchange striction mechanism.

In spite of other mechanisms proposed, the above two have been well recognized for most multiferroics of noncollinear and collinear spin orders, in particular for orthorhombic manganites  $\text{RMnO}_3$  with R being rare-earth.<sup>3</sup> Two generic characteristics associated with the spin order induced polarization  $P$  as functions of  $T$  and magnetic field  $H$  can be highlighted. First, both the noncollinear and collinear spin orders are the compromises of multifold exchange competition which enables the spin structure highly frustrated. This leads to, in a usual way, a sequence of spin ordering starting from commensurate (C) and incommensurate (IC) antiferromagnetic (AFM) orders with noncollinear or collinear alignment becomes possible and is often identified in multiferroic oxides such as manganites, ferrites, cobaltates, vanadates, cuprates, etc.<sup>3,12</sup> It certainly implies that the temperatures for these spin orderings are low, and so is the FE Curie point ( $T_C$ ). Obviously, driving the transitions between these spin orders does not need much additional exchange energy on cost of lattice distortion energy for ferroelectricity, implying that the as-generated electric polarization must be small either. In consequence, the measured  $P(T)$  curve would exhibit anomalies at these ordering points. Second, these spin orders are not robust against intrinsic and external stimuli due to the strong spin frustration, which can be well illustrated by the giant magnetoelectric response. Even though, the two mechanisms show distinct difference in terms of the response, and the DMI induced polarization is quite sensitive to  $H$  but the exchange striction induced one is not. Surely, details of such responses can be fascinating and materials dependent, and readers may consult recent review papers.<sup>1,3,4,10</sup>

Apart from the two generic aspects, reality is that many more observed phenomena cannot be reasonably understood within the two respect frameworks. One issue to be covered in this mini-review is the very different FE behaviors in

compounds with coexisting  $4f$  and  $3d$  moments.<sup>20–23</sup> Without losing the generality, one may take the well-known multiferroic manganite  $\text{DyMnO}_3$  as an example. First, this material has two kinds of moments:  $3d\text{-Mn}^{3+}$  and  $4f\text{-Dy}^{3+}$ , which unfortunately add complexity to the two mechanisms for ferroelectricity generation and are appreciated due to involvement of additional physics.<sup>21,22</sup> Second, the  $3d\text{-}4f$  coupling in  $\text{DyMnO}_3$  is quite strong, which makes the Mn and Dy spin ordering sequences quite different.<sup>20,24</sup> It is known that the  $4f$  moments in rare-earth oxides free of  $3d$  moments may not order until extremely low temperature ( $T < 1.0\text{K}$ ).<sup>25,26</sup> One assigns this ordering temperature as  $T_{\text{Dy}}$  for  $\text{DyMnO}_3$  (also  $\text{DyMn}_2\text{O}_5$  to be discussed here). However, this ordering in  $\text{DyMnO}_3$  occurs at a much higher temperature  $T_{\text{Dy}} \sim 10\text{K}$ , which is believed to be driven by the strong Dy–Mn coupling, given that the Mn spins begin to order at  $\sim 40\text{K}$  or higher.<sup>22,24</sup> An immediate consequence is not only the much higher  $T_{\text{Dy}}$ , but more importantly the coherent Dy spin ordering at  $T \gg T_{\text{Dy}}$ , induced by the Dy–Mn coupling. For  $\text{DyMnO}_3$ , this coherence results in the  $\uparrow\uparrow\downarrow\downarrow$  Mn–Dy–Mn–Dy $\cdots$  spin alignment along the  $c$ -axis in the  $bc$ -plane, while the Mn spiral spin structure has its spiral wavevector along the  $b$ -axis.<sup>22</sup> This specific Mn and Dy coherent spin structure allows the co-existence of two FE sublattices generated respectively from the DMI mechanism ( $P_{\text{Mn}}$  sublattice) and exchange striction one ( $P_{\text{Dy}}$  sublattice).<sup>22,27–29</sup> Fortunately, the two components both align along the  $c$ -axis, enabling  $\text{DyMnO}_3$  to be a system with the largest polarization  $P = P_{\text{Mn}} + P_{\text{Dy}}$  ever observed in orthorhombic  $\text{RMnO}_3$ . The relevant physics can be illustrated in Fig. 2 and details can be found in an earlier paper.<sup>29</sup>

$\text{DyMnO}_3$  represents the first ever measured multiferroic compound where two FE sublattices coexist and coherently contribute to the total polarization which exhibits an unusual  $T$ -dependence, as shown in Fig. 2 (bottom).<sup>29</sup> It is usually believed that two coexisting FE sublattices most likely favor an antiparallel alignment, leading to an antiferroelectric (AFE) or ferrielectric (FIE) lattice, as often found in normal FEs.<sup>30,31</sup> For a reference, a FIE lattice and its  $T$ -dependent

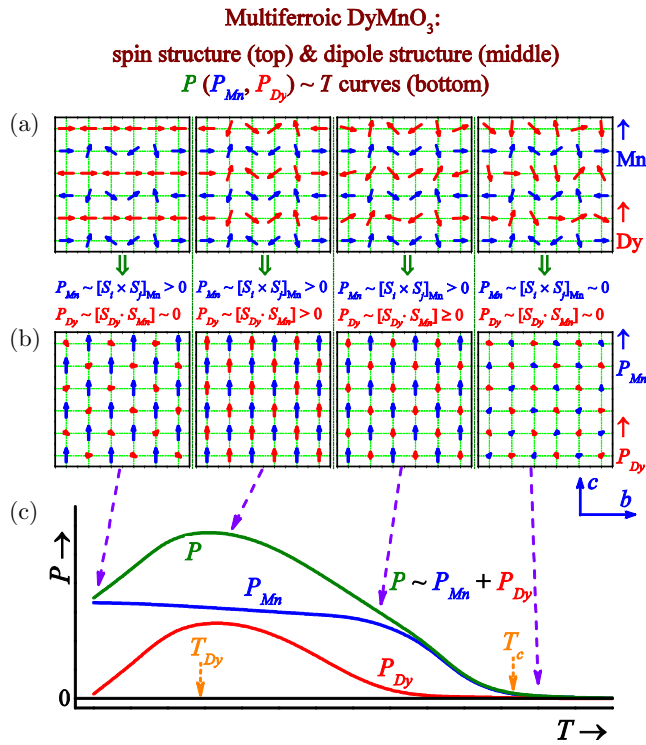


Fig. 2. (Color online) Well-recognized multiferric scenario for DyMnO<sub>3</sub> with both 4*f* Dy<sup>3+</sup> spins and 4*d* Mn<sup>3+</sup> spins.<sup>29</sup> (a) The spin structures on the *bc*-plane at four different *T* as indicated in (c). (b) The as-generated two FE sublattices *P*<sub>Mn</sub> and *P*<sub>Dy</sub> at the four *T*, respectively. The *P*<sub>Mn</sub> sublattice is generated via the DMI mechanism ( $P_{Mn} \sim [S_i \times S_j]_{Mn}$ ) and the *P*<sub>Dy</sub> sublattice is generated via the exchange striction ( $P_{Dy} \sim [S_{Dy} \cdot S_{Mn}]$ ), as respectively shown in Fig. 1. (c) The proposed *P*<sub>Mn</sub>, *P*<sub>Dy</sub>, and *P* = *P*<sub>Mn</sub> + *P*<sub>Dy</sub> as a function of *T*, respectively.

polarization are schematically shown in Fig. 3 where the two FE sublattices (blue and red) have different ordering temperatures, leading to a crossover from *P* < 0 to *P* > 0 (*P* = *P*<sub>+</sub> + *P*<sub>−</sub>) upon decreasing *T*. This crossover is a prime characteristic for a FIE lattice.

An immediate motivation to this end is whether any FIE multiferric is available or not. In fact, this issue was once concerned when another class of multiferric manganites RMn<sub>2</sub>O<sub>5</sub> was claimed to exhibit ferroelectricity. As early as 2004, DyMn<sub>2</sub>O<sub>5</sub> was observed to exhibit a clear crossover of its *P*(*T*) behavior (*P* along the *b*-axis) and was argued to be a FIE system,<sup>32</sup> while this phenomenon was not well characterized until recently.<sup>33,34</sup> Based on the knowledge of the ferroelectricity in DyMnO<sub>3</sub>,<sup>29</sup> one has sufficient reason to expect possible AFE or FIE behavior in DyMn<sub>2</sub>O<sub>5</sub>. First, DyMn<sub>2</sub>O<sub>5</sub> also has 3*d* and 4*f* moments: Mn and Dy ions, and strong Dy–Mn coupling is well confirmed.<sup>35–40</sup> More than this, here Mn has two valence states: Mn<sup>3+</sup> and Mn<sup>4+</sup>, implying the Dy<sup>3+</sup>–Mn<sup>3+</sup> and Dy<sup>3+</sup>–Mn<sup>4+</sup> couplings in addition to the 3*d* and 4*f* exchange interactions themselves. Such multifold coupling may bring more possibilities for two

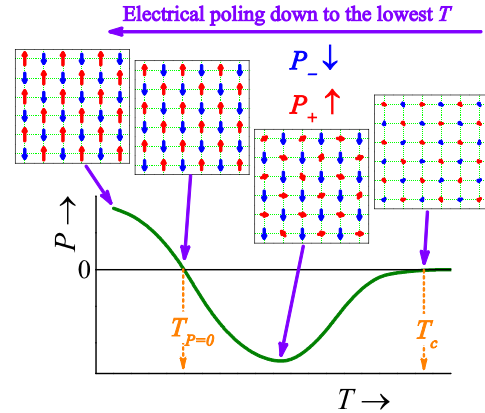


Fig. 3. (Color online) The polarization *P* in a FIE upon decreasing *T* down to the negative–positive crossover point *T*<sub>*P*=0</sub>. The FIE lattice consisting of two FE sublattices *P*<sub>+</sub> and *P*<sub>−</sub> at four different *T* are inserted for guide of eyes.

or more FE sublattices to develop. Second, a remarkable perturbation of polarization *P* in response to complicated magnetic ordering sequence was identified, suggesting more than one polarization component in DyMn<sub>2</sub>O<sub>5</sub>.<sup>32–34,41–43</sup> Third, recent investigations based on extensive neutron scattering and resonant X-ray scattering data disclosed the magnetic structure and its transitions, tampering a basis to find a correlation between spin structure and FE polarization.<sup>35–43</sup> Finally, some RMn<sub>2</sub>O<sub>5</sub> members other than DyMn<sub>2</sub>O<sub>5</sub> (R=Ga, Tb, Ho, Er, Tm, Y, Bi, etc.) have been repeatedly revealed to be multiferrics and their polarizations show unusual behaviors too,<sup>32,33,35,37,39,43–48</sup> suggesting that ferrielectricity may be a common characteristic of some members of this family.

In the last several years, various attempts to figure out the microscopic origins for ferroelectricity in DyMn<sub>2</sub>O<sub>5</sub> have been made<sup>32–34,41–43</sup> and so far available data demonstrate the ferrielectricity in DyMn<sub>2</sub>O<sub>5</sub> in a self-consistent manner. Several aspects were carefully investigated, addressing the pure, Mn-site substituted, and Dy-site substituted DyMn<sub>2</sub>O<sub>5</sub>.<sup>49,50</sup> The major features associated with the ferrielectricity of pure DyMn<sub>2</sub>O<sub>5</sub> were sorted out. Our strategy was to start from these features and propose a phenomenological framework.<sup>34</sup> The subsequent Mn-site and Dy-site substitution experiments were designed to check this framework.<sup>49,50</sup> In this mini-review, we intend to present all our data on the multiferricity of DyMn<sub>2</sub>O<sub>5</sub> in an integrated package, eventually revealing the FIE nature of DyMn<sub>2</sub>O<sub>5</sub>. The remaining part is organized as follows. In Sec. 2 are outlined the crystal structure, magnetism, dielectric and FE behaviors, and discussion on the underlying mechanisms for multiferricity in literature on RMn<sub>2</sub>O<sub>5</sub> and particularly DyMn<sub>2</sub>O<sub>5</sub>. Our improved experiments on polarization *P* as a function of *T* and *H* and proposed FIE lattice model will be discussed in Sec. 3. Subsequently, measured data on substitution trials at the Mn site and Dy site in order to validate this

model will be described in Secs. 4 and 5. The conclusion and perspectives will be presented in Sec. 6.

## 2. State-of-the-Art on Multiferroicity in $\text{DyMn}_2\text{O}_5$

### 2.1. Crystal structure

All known  $\text{RMn}_2\text{O}_5$  members have the same orthorhombic crystal structure of the  $Pbam$  space group at low  $T$  ( $< 43$  K),<sup>35,39,46</sup> while details of the lattice distortion depend on the R ionic size. The structural complexity is remarkably simplified by the well-demonstrated built-in ordered ionic occupation and thus the charge order. The lattice consists of two types of alternatively stacked structural units. One is the square pyramid where five oxygen ions occupy the corners and  $\text{Mn}^{3+}$  occupies the center (not exactly at the center but shifted towards the square base). The other is the octahedral unit in which  $\text{Mn}^{4+}$  takes the center position. On the  $ab$ -plane, the two structural units are corner-sharing via either the base or apex of the pyramids, while two neighboring pyramids contact via the base. Along the  $c$ -axis, the octahedral units align via the edge sharing and constitute the  $c$ -oriented  $\text{Mn}^{4+}$ – $\text{Mn}^{4+}$  chains where the  $\text{Mn}^{4+}$  coordinate along the  $c$ -axis is  $z_1 \sim 0.25$  (or  $z_1 \sim 0.75$ ). The  $c$ -axis coordinate of  $\text{Mn}^{3+}$  in pyramid units is  $z_2 \sim 0.50$ .<sup>39</sup> This implies that the lattice consists of alternatively stacked  $\text{Mn}^{4+}\text{O}_6$  octahedral planes at  $z_1 \sim 0.25$ ,  $\text{Mn}^{3+}\text{O}_5$  pyramidal planes at  $z_2 \sim 0.50$ , and  $\text{Mn}^{4+}\text{O}_6$  octahedral planes at  $z_1 \sim 0.75$  along the  $c$ -axis. The R ions occupy the empty space of the  $\text{MnO}_6$  octahedral and  $\text{MnO}_5$  pyramidal network, coordinating roughly at  $z_1 \sim 0.0$  and  $z_2 \sim 1.0$  along the  $c$ -axis, i.e., roughly on the  $\text{MnO}_6$  octahedral planes. Therefore, the ionic stacking sequence along the  $c$ -axis is  $\text{Dy}^{3+}$ – $\text{Mn}^{4+}$ – $\text{Mn}^{3+}$ – $\text{Dy}^{3+}$ – $\text{Mn}^{4+}$ – $\text{Mn}^{3+}$ – $\dots$ .

If such a lattice geometry applies to  $\text{DyMn}_2\text{O}_5$ , the as-generated lattice structure can be schematically drawn in Fig. 4(a) for a guide of eyes.<sup>35–42</sup> The  $ab$ -plane projected pattern is shown in Fig. 4(b) where the Dy and Mn spins are labeled as color arrows and the oxygen ions are ignored. It is seen that the two sets of pyramids and octahedra (gray and light-gray groups) constitute the plane network and the  $\text{Dy}^{3+}$  ions occupy the empty space (white). There is a  $c/4$  shift ( $c$  is the  $c$ -axis lattice constant) between the light-gray and gray sets of pyramids and octahedra, and for each set, the pyramids also have a  $c/4$  shift with respect to the octahedra. In spite of the structure complexity, the projected  $ab$ -plane block configuration shown in Fig. 4(b) can be the basis for discussion on magnetism and ferroelectricity of  $\text{DyMn}_2\text{O}_5$ .

### 2.2. Magnetic ordering and spin structure

The magnetic structures of  $\text{RMn}_2\text{O}_5$ , in particular that of  $\text{DyMn}_2\text{O}_5$ , have been extensively investigated mainly using neutron diffraction and resonant X-ray scattering techniques.<sup>36,38–42</sup> As expected, a series of IC-AFM and C-AFM

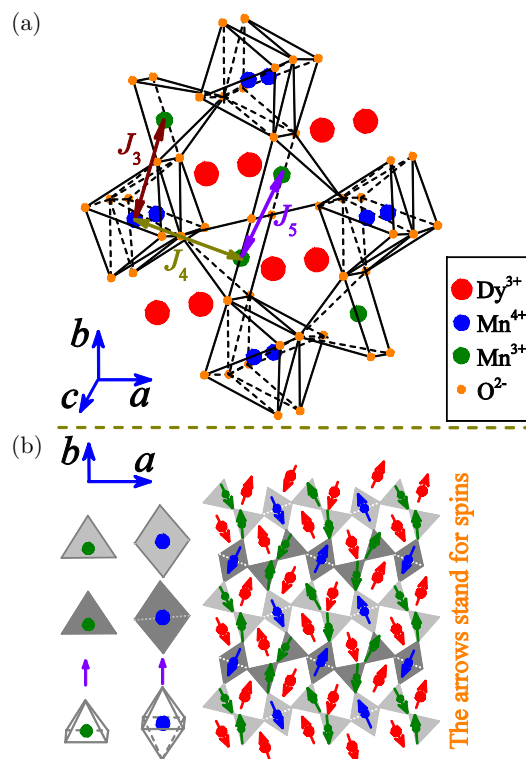


Fig. 4. (Color online) The lattice structure of  $\text{DyMn}_2\text{O}_5$  (a), and  $ab$ -plane projected lattice with  $\text{Dy}^{3+}$ ,  $\text{Mn}^{3+}$ , and  $\text{Mn}^{4+}$  spins denoted by color arrows (b). The  $\text{Mn}^{4+}\text{O}_6$  octahedra and  $\text{Mn}^{3+}\text{O}_5$  pyramids are drawn only for guide of eyes.

ordering events of Mn spins is discovered upon decreasing  $T$  from  $T_{N0} \sim 43$  K, above which the magnetic structure is paramagnetic (PM) with no ferroelectricity. If R is magnetic, the spin ordering can be more complicated. For  $\text{DyMn}_2\text{O}_5$  where the  $\text{Dy}^{3+}$  moment is  $\sim 10 \mu_B$ , the  $\text{Mn}^{3+}/\text{Mn}^{4+}$  PM phase transits into an IC-AFM phase below  $T_{N0}$ , entering a C-AFM phase below  $T_{N1} \sim 40$  K which was found to be FE. Subsequently, two phase transitions at  $T_{N2} \sim 28$  K and  $T_{N3} \sim 20$  K were identified, accompanied with the gradual C-AFM to IC-AFM transitions until  $T_{N3}$  below which the C-AFM phase disappears. The two phases are both FE but the dielectric permeability and electric polarization at these points show strong anomalies.<sup>36,41</sup> To the end, again a magnetic transition at  $T_{\text{Dy}} \sim 9$  K was observed, which is believed to arise from the additional Dy spin ordering into a C-AFM phase plus the sustained Mn IC-AFM phase. This additional ordering is driven by the  $4f$ – $4f$  (Dy–Dy) interactions, as well recognized in many rare-earth oxides.<sup>25,26</sup>

Up to date, it remains unclear whether the magnetic transitions at  $T_{N2}$  and  $T_{N3}$  are related to the Dy spin ordering or not. Most likely they are driven by the  $\text{Dy}^{3+}$ – $\text{Mn}^{4+}$  and  $\text{Dy}^{3+}$ – $\text{Mn}^{3+}$  couplings, given that the  $\text{Dy}^{3+}$ – $\text{Mn}^{4+}$  separation shorter than the  $\text{Dy}^{3+}$ – $\text{Mn}^{3+}$  distance may favor a stronger Dy–Mn coupling. The consecutive magnetic transitions can be qualitatively explained by the competing interactions. The three major Mn–Mn exchange terms are denoted



as  $J_3$ ,  $J_4$ , and  $J_5$  in Fig. 4(a),<sup>39</sup> while the minor  $\text{Mn}^{4+}$ – $\text{Mn}^{4+}$ ,  $\text{Dy}^{3+}$ – $\text{Mn}^{4+}$ , and  $\text{Dy}^{3+}$ – $\text{Mn}^{3+}$  exchanges cannot be neglected either. These exchange interactions together with the relevant frustrations and anisotropies were discussed in detail but only qualitatively.<sup>35–42</sup>

Nevertheless, it is interesting to find that almost all  $\text{RMn}_2\text{O}_5$  members with strong ferroelectricity exhibit nearly identical spin structure if the R moments are not considered.<sup>39</sup> Otherwise, the structure can be slightly different, particularly in the low- $T$  range where the Dy spin ordering appears, as shown in Fig. 4(b) for  $\text{DyMn}_2\text{O}_5$ .<sup>35–42</sup> First, all the Mn spins have the major components lying on the  $ab$ -plane, implying that the in-plane anisotropy is dominant and the out-of-plane one is relatively weak. Second, the in-plane Mn spins are roughly collinear although the noncollinear components cannot be negligible.<sup>51</sup> It seems that the collinear components align along the  $b$ -axis for  $\text{DyMn}_2\text{O}_5$  but along the  $a$ -axis for other  $\text{RMn}_2\text{O}_5$  members. The minor noncollinear alignment was claimed to be attributed to the competition between the exchanges and the DMI. Considering the DMI mechanism for ferroelectricity, this noncollinear issue was discussed but no sufficient evidence echoing the major role of the DMI has been settled down.<sup>51</sup> Third, the Dy spins also favor the collinear alignment with the Mn spins below  $T_{N2}$  and  $T_{N3}$ , as shown in Fig. 4(b) too. The major collinear Dy spin structure developed above  $T_{\text{Dy}}$  makes the Dy spin re-ordering at  $T_{\text{Dy}}$  less essential in terms of ferroelectricity. It is thus suggested that this Dy re-ordering may even benefit to the ferroelectricity, different from the case of  $\text{DyMnO}_3$ .

### 2.3. Ferroelectricity and magnetoelectric responses

The ferroelectricity in  $\text{RMn}_2\text{O}_5$  and its magnetic origin have been highly concerned since the discovery of ferroelectricity in  $\text{HoMn}_2\text{O}_5$ ,  $\text{DyMn}_2\text{O}_5$ , and  $\text{TbMn}_2\text{O}_5$ .<sup>51–64</sup> Phenomenological theories on electric polarization has been developed, whose predictions seem to be qualitatively consistent with experimental results.<sup>65–67</sup> If only the  $\text{Mn}^{3+}$  and  $\text{Mn}^{4+}$  spins are considered, the polarization is believed to be generated via the second mechanism shown in Fig. 1(b). The exchange striction effect arises from the three-spin blocks, as schematically drawn in Fig. 5 where the open dots represent the  $\text{Mn}^{3+}$  ions without exchange interactions. Despite the nearly collinear Mn spin ordering may take different configurations with two examples shown in Figs. 5(a) and 5(b), the exchange striction induced  $\text{Mn}^{3+}$  ionic displacements with respect to  $\text{Mn}^{4+}$  are majorly along the  $b$ -axis, leading to polarization  $P_{\text{Mn}}$  roughly aligned along the  $b$ -axis too. Based on this mechanism, a consensus on the ferroelectricity has been reached regarding the following several issues, while some issues remain unclear.<sup>51–64</sup>

- (1) No matter magnetic or nonmagnetic R, all the multiferroic  $\text{RMn}_2\text{O}_5$  members have their polarization along

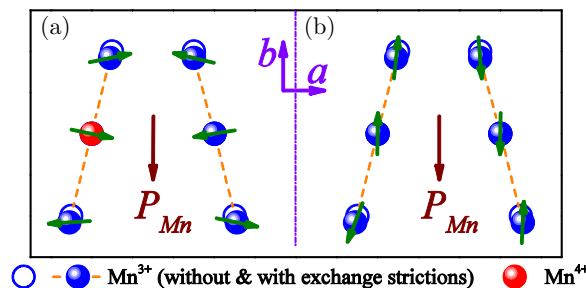


Fig. 5. (Color online) The exchange striction induced local polarization  $P_{\text{Mn}}$  in  $\text{RMn}_2\text{O}_5$  where the R spin if any is ignored. (a) The three ion blocks with roughly  $\leftarrow\leftrightarrow$  ( $\rightarrow\leftrightarrow$ ) spin chains and (b) the three ion blocks with roughly  $\uparrow\uparrow$  ( $\downarrow\downarrow$ ) spin chains. The solid (open) dots represent the ionic sites considering (ignoring) the exchange striction effect, with the  $\text{Mn}^{4+}$  ion as reference position in each block.

the  $b$ -axis without exception. A connection of this property with the spin structures allows an argument that the polarization is essentially generated by the collinear Mn moments while the noncollinear moments play only minor roles if any.

- (2) For all the cases, polarization  $P$  enters right below  $T_{N1}$  and exhibits anomalous variations at those magnetic ordering temperatures (e.g., at  $T_{N2}$  or  $T_{N3}$  for  $\text{DyMn}_2\text{O}_5$ ), reflecting the intimate correlation between the spin structure and ionic displacement. This effect is particularly remarkable as R is magnetic, suggesting the substantial roles of the  $4f$  electrons.
- (3) Regarding the responses of  $P$  and dielectric permeability ( $\epsilon$ ) to  $H$ , it has nearly no exception that remarkable  $P(H)$  and  $\epsilon(H)$  responses can be observed only in the low- $T$  range, typically below  $\sim 20$  K (below  $T_{N2}$  for  $\text{DyMn}_2\text{O}_5$ ), at least for the cases under weak magnetic stimulation. Interestingly, one can find that the low- $T$  response, if any, is strong in those members with strongly magnetic R. It implies once more the essential roles of the R moments in determining the multiferroicity of  $\text{RMn}_2\text{O}_5$ , which is an issue less concerned so far but will be addressed in this mini-review.

Nevertheless, more than the reached consensus issues are those inconsistent and unclear issues. We highlight here several major but yet confusing points. For illustration convenience, one focuses on the  $P(T)$  data, whose qualitative features are presented in Fig. 6 for a guide of eyes. It is noted that these data were measured by means of two different techniques, i.e., the Pyro method and Poling method,<sup>32,41</sup> which will be discussed later. We highlight those unclear issues first.

- (1) Very different  $P(T)$  dependences were identified for different  $\text{RMn}_2\text{O}_5$  members, leaving puzzling on the complicated physics associated with ferroelectricity. These puzzles are more or less related to the techniques

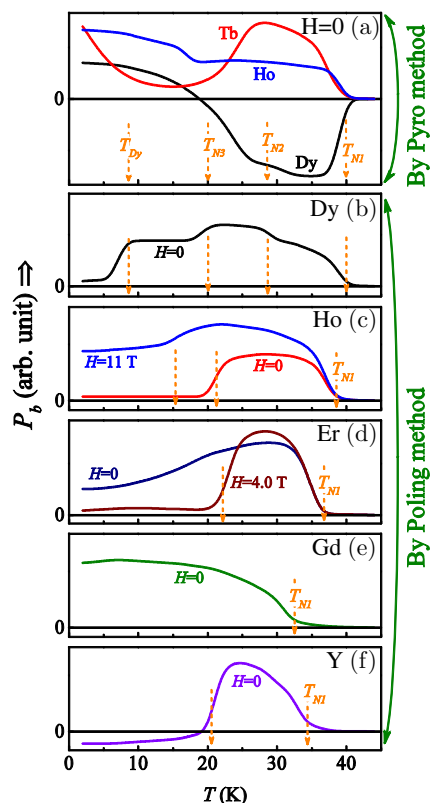


Fig. 6. (Color online) Schematic traces of measured polarization  $P(T)$  data along the  $b$ -axis for  $\text{RMn}_2\text{O}_5$ : (a)  $\text{R}=\text{Dy}$ ,  $\text{Tb}$ , and  $\text{Ho}$ ; (b)  $\text{R}=\text{Dy}$ ; (c)  $\text{R}=\text{Ho}$ ; (d)  $\text{R}=\text{Er}$ ; (e)  $\text{R}=\text{Gd}$ ; (f)  $\text{R}=\text{Y}$ ; respectively.<sup>32,41,48,64</sup> The methods (Pyro method and Poling method) for measuring the polarizations are marked aside. The magnetic field applied for the measurement in each case is labeled.

used for probing the  $P(T)$  dependences. These distinct differences are shown in Fig. 6(a) for  $\text{R}=\text{Ho}$ ,  $\text{Dy}$ , and  $\text{Tb}$ , where the three curves are taken from the data in Ref. 32 obtained using the Pyro method and those  $T_{N1}$ ,  $T_{N2}$ ,  $T_{N3}$ , and  $T_{\text{Dy}}$  are referred to  $\text{DyMn}_2\text{O}_5$ . This was the first time to report the FIE-like behavior for  $\text{DyMn}_2\text{O}_5$ , while the  $P(T)$  dependences for  $\text{HoMn}_2\text{O}_5$  and  $\text{TbMn}_2\text{O}_5$  are unusual too.

- (2) Given the Poling method used for measurements,<sup>41</sup> the  $P(T)$  dependences of different members also show distinct differences, as shown in Figs. 6(b)–6(f).  $\text{DyMn}_2\text{O}_5$  does show several clear anomalies at  $T_{N1}$ ,  $T_{N2}$ ,  $T_{N3}$ , and  $T_{\text{Dy}}$ .<sup>41</sup> The polarization of  $\text{HoMn}_2\text{O}_5$  becomes nearly disappeared below  $\sim 20$  K,<sup>68</sup> while  $\text{GdMn}_2\text{O}_5$  does not.<sup>48</sup> The most surprising is the positive-to-negative crossover of  $P$  at  $T \sim 20$  K for  $\text{YMn}_2\text{O}_5$ ,<sup>64</sup> noting that  $\text{Y}$  is non-magnetic.
- (3) While magnetoelectric response of  $\text{RMn}_2\text{O}_5$  in terms of response of  $P$  to  $H$  is known to be weak, which is true in the high- $T$  range, very remarkable responses are identified in the low- $T$  range. A sufficiently high  $H$  can trigger off large low- $T$  polarization for  $\text{HoMn}_2\text{O}_5$  but suppress the low- $T$  polarization for  $\text{ErMn}_2\text{O}_5$ .<sup>68</sup>

- (4) Continuous debate on the reason for nearly zero polarization in  $\text{DyMn}_2\text{O}_5$  below  $T_{\text{Dy}}$  remains, so does it for  $\text{HoMn}_2\text{O}_5$  below  $\sim 20$  K.<sup>34,41</sup> The “non-FE” phase below  $T_{\text{Dy}}$  for  $\text{DyMn}_2\text{O}_5$  is called the X-phase. While  $\text{Dy}$  moment is big and believed to couple strongly with  $\text{Mn}$  moment, leading to destruction of the  $\text{Mn}$  spin exchange striction effect, no such phenomenon is observed in  $\text{GdMn}_2\text{O}_5$  where the  $\text{Gd}$ – $\text{Mn}$  coupling is also strong.<sup>48</sup>

In short, a general scenario for ferroelectricity in  $\text{RMn}_2\text{O}_5$  family seems unavailable at this stage, and a case-by-case checking on each member is needed.<sup>39</sup> In addition, the confusing issue of polarization measurement should be concerned since the two methods do prepare very different data. Finally, it should be mentioned that ferroelectricity in multiferroic oxides with strong electron correlations has both the electronic and ionic contributions.<sup>31</sup> In some cases, one may be negligible with respect to the other, while the two contributions are comparable and even cancelled in other cases. The latter was predicted in  $\text{HoMn}_2\text{O}_5$  by first principles calculations recently.<sup>69</sup> In the present study, this issue will not be addressed, but it can be a critical ingredient for the physics of ferroelectricity in multiferroics.

#### 2.4. Comments on polarization measurements

As mentioned above, so far available data on polarization  $P$  as a function of  $T$  and  $H$  were measured mainly by means of two techniques. The first is the conventional pyroelectric current (Pyro) method, which has been extensively used in measuring  $P(T, H)$  for multiferroics with small  $P$  (as small as  $\sim 1.0 \mu\text{C}/\text{m}^2$ ) and low transition temperature. A schematic illustration of the Pyro method is given in Fig. 7(a). The sample covered with the top and bottom electrodes (e.g., Au) is submitted to electric poling under a field  $E_{\text{pole}}$  during the cooling run until  $T = T_{\text{end}}$ , and then electrically short-circuited for sufficient time at  $T_{\text{end}}$ . The  $T_{\text{end}}$  should be as low as possible and for typical case  $T_{\text{end}} = 2$  K. The released current  $I_{\text{pyro}}$  from the sample under zero electric bias is probed during the subsequent warming run from  $T_{\text{end}}$  up to an assigned temperature  $T_0$ . The  $I_{\text{pyro}}(T)$  is integrated from  $T_0$  down to  $T_{\text{end}}$ , generating polarization  $P$  as a function of  $T$ . The Pyro method is applicable only if  $P$  at  $T_{\text{end}}$  is nonzero, otherwise the electric poling down to  $T_{\text{end}}$  is almost ineffective even if  $P$  is nonzero at any  $T$  other than  $T_{\text{end}}$ .

The second is the Poling method, as drawn in Fig. 7(b). Instead of the separated poling and probing steps, here the poling and probing are carried out simultaneously. The sample under a poling field  $E_{\text{pole}}$  is gradually cooled down to  $T_{\text{end}}$  from a high  $T$  during which the total current  $I_{\text{tot}}$  across the sample is probed. This field is supposed to be small sufficiently so that the field induced leaky current  $I_{\text{leaky}}$  is much smaller than  $I_{\text{pyro}}$  over the whole  $T$ -range. A proper fitting procedure may allow an exclusion of  $I_{\text{leaky}}$ , leaving  $I_{\text{pyro}}(T)$  and thus  $P(T)$  to be evaluated. An immediate question is the validity of assumption  $I_{\text{leaky}} \ll I_{\text{pyro}}$ , which may

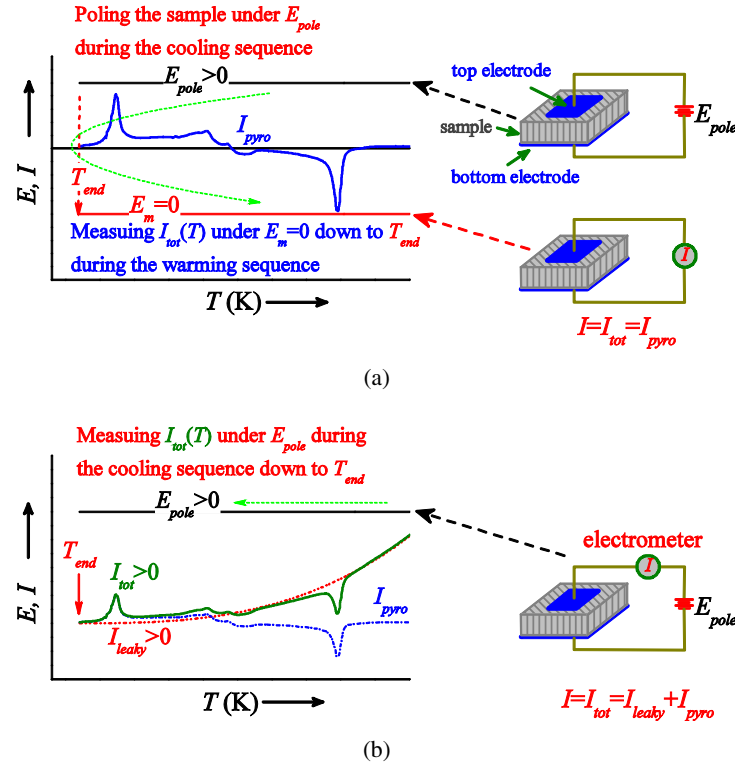


Fig. 7. (Color online) Schematic drawing of the (a) Pyro method and (b) Poling method for probing polarization  $P$ . In the Pyro method, the electrode-coated sample is pre-poled electrically from a sufficiently high  $T$  down to a given  $T_{\text{end}}$  at which the electric field  $E_{\text{pole}}$  is removed, followed by a sufficiently long time electric short-circuiting of the sample. Then the sample is slowly warmed up from  $T_{\text{end}}$  during which the pyroelectric current  $I_{\text{pyro}}$  released from the two electrodes is collected. In the Poling method, a low electric field  $E_{\text{pole}}$  is applied to the electrode-coated sample from a sufficiently high  $T$ , followed by a slow cooling of the sample during which the current passing across the sample is collected. Then an author-dependent procedure is taken to separate the leaky current and polarized current, so that polarization  $P$  can be obtained from the polarized current data.

not be always true for  $\text{RMn}_2\text{O}_5$ , since a small  $E_{\text{pole}}$  implies an incomplete poling of the sample and thus the evaluated  $P$  may not be the saturated one. Furthermore, a separation of  $I_{\text{pyro}}$  from  $I_{\text{tot}}$  is anyway a matter if the dependences  $I_{\text{leaky}}(T)$  and  $I_{\text{pyro}}(T)$  are unknown. In fact, Higashiyama *et al.* discussed these issues in their work.<sup>41</sup> The problem here for  $\text{RMn}_2\text{O}_5$  is that this method may not identify correctly the FIE state.

Given the above discussion, we again come back to the Pyro method and have applied it for careful measurements of the released  $I_{\text{pyro}}(T)$  data, noting that our Pyro technique is of precision as high as 0.05 pA. The details of experiments covered in this mini-review can be found in earlier literature, including samples synthesis, microstructural characterizations, and measurements on thermodynamic, magnetic, and electric properties, which will not be described here any more.

### 3. Results on $\text{DyMn}_2\text{O}_5$

Our data reported here are on well-prepared polycrystalline  $\text{DyMn}_2\text{O}_5$  samples,<sup>34</sup> while data reported in literature on single crystals are taken for comparison. Since special emphasis will be oriented onto the Mn- and Dy-sites

substitutions, a preparation of whole set of single-crystal samples is challenging, and polycrystalline samples are much easier to access.

#### 3.1. Magnetic and electric characterizations

The magnetic ordering sequence can be sensitively probed by specific heat data ( $C_p$ ), while magnetization data are insensitive to the Mn spin ordering due to that the magnetic signals are mainly from the Dy moments much stronger than Mn moments. The  $T$ -normalized specific heat ( $C_p/T$ ) and  $M$  as a function of  $T$  are plotted in Figs. 8(a) and 8(b), respectively. Earlier determined magnetic ordering points  $T_{N1}$ ,  $T_{N2}$ ,  $T_{N3}$ , and  $T_{Dy}$  are labeled and the assigned paraelectric (PE), ferroelectric (FE1, FE2, FE3), and X phase regions are marked too for reference, where differences of the three FE phases (FE1, FE2, FE3) remain unclear and the X phase was claimed to be non-FE.<sup>41</sup> It is seen that the  $C_p/T(T)$  curve shows clear anomalies at these points, while the  $M(T)$  curve exhibits no anomaly except the broad peak at  $\sim T_{Dy}$ , reflecting gradual Dy spin ordering proceeding over the broad  $T$ -range in the low- $T$  range (below  $T_{N2}$  or  $T_{N3}$ ).

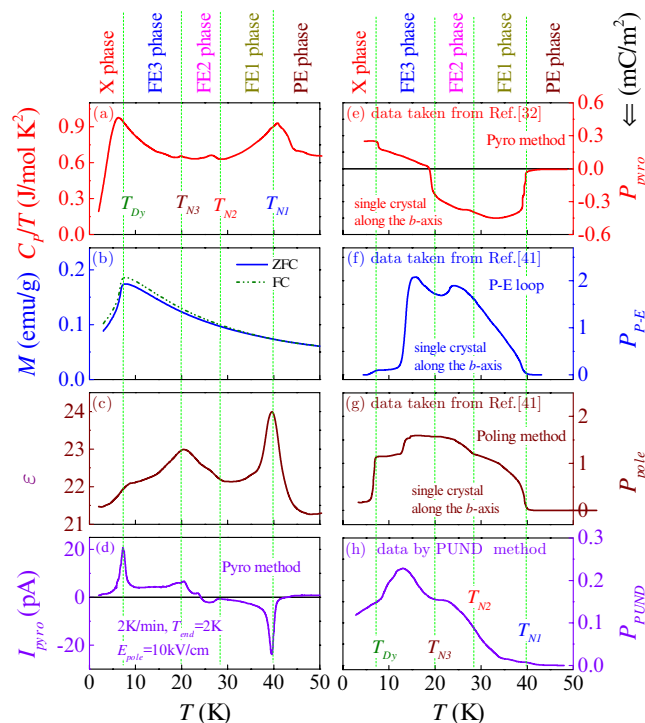


Fig. 8. (Color online) Measured  $T$ -normalized specific heat  $C_p/T$  (a),  $dc$  magnetization  $M$  under zero-field cooled (ZFC) and field cooling (FC) modes with measuring field of  $\sim 1000$  Oe (b), dielectric permeability  $\varepsilon$  at 10 kHz under  $ac$  signal of 50 mV (c), and pyroelectric current  $I_{pyro}$  (d) for polycrystalline  $DyMn_2O_5$ , as a function of  $T$ , respectively. The measured polarizations as a function of  $T$  respectively taken from Ref. 32 using the Pyro method (e), from Ref. 41 using the  $P$ - $E$  loop method (f), from Ref. 41 using the Poling method (g), and measured using the PUND method (h), respectively, are presented for comparison. The data in (e)–(g) were obtained for  $DyMn_2O_5$  single crystal samples.

The magnetic ordering can also find sensitive response in dielectric permeability ( $\varepsilon$ ), as shown in Fig. 8(c). The strongest anomaly at  $\sim T_{N1}$  and broad peak at  $\sim T_{N3}$  suggest the FE transitions. The transition at  $\sim T_{N1}$  can be tentatively assigned as the consequence of the collinear Mn spin ordering and that at  $\sim T_{N3}$  marks the induced Dy spin ordering in coherence with the Mn order. The anomalies at  $\sim T_{N2}$  and  $\sim T_{Dy}$  are relatively weak, indicating the minor variations of polarization  $P$  at these points. In particular, the small bump at  $\sim T_{Dy}$  reflects the variation of  $P$  due to the Dy spin ordering driven by the Dy–Dy exchange interaction which is no longer negligible at low  $T$ .

The  $I_{pyro}(T)$  is also sensitive to these spin orderings, and the data are plotted in Fig. 8(d). The one-to-one correspondence among the  $I_{pyro}(T)$  peaks, the  $\varepsilon(T)$  peaks, and the  $C_p/T(T)$  anomalies is clearly identified, suggesting that the  $I_{pyro}$  signals are indeed from the variation of  $P$  on one hand and the pyroelectric current may be one of the most sensitive parameters to magnetic ordering in multiferroics on the other hand. Here, more significant are the negative peak at  $\sim T_{N1}$

and the positive peaks at  $\sim T_{N3}$  and  $T_{Dy}$ , immediately allowing an argument that  $DyMn_2O_5$  may be a FIE rather than a FE.

In addition, the  $P(T)$  data in earlier reports from various groups are reproduced for comparison purpose, as shown in Figs. 8(e)–8(h). The data in Fig. 8(e) are from Ref. 32 obtained using the Pyro method, showing the negative–positive crossover of  $P$  roughly at  $\sim T_{N3}$ , consistent with our results. It is noted that the assigned X phase has nonzero  $P$ , suggesting that it is FE. The  $P(T)$  data in Figs. 8(f)–8(h) were obtained using the modified  $P$ - $E$  loop method from Ref. 41, the Poling method from Ref. 41, and the so-called positive-up and negative-down (PUND) method<sup>60</sup> in our group on polycrystalline sample, respectively. For these cases, the measured  $P$  must be positive since the measurements were performed under an electric bias. Even though, one sees various features of these  $P(T)$  curves around  $\sim T_{N1}$ ,  $T_{N2}$ ,  $T_{N3}$ , and  $T_{Dy}$ . These methods basically cannot identify the ferrielectricity if any, but the  $P$  in the low- $T$  range is indeed small. In fact, no clear explanations for these features have been available so far. In short summary, there appears substantial difference between the results obtained using different methods, appealing for more careful handle of these issues. This is the reason for us to come back to the Pyro method which can more reliably and precisely probe the pyroelectric current without the electric bias induced leaky current and other activations.

Subsequently, the measured  $I_{pyro}(T)$  data at three different warming rates (2, 4, 6 K/min) are plotted in Figs. 9(a)–9(c), given  $E_{pole} = 10$  kV/cm. The three  $I_{pyro}(T)$  curves almost overlap onto a master curve, demonstrating that the current is indeed from the pyroelectric effect. Furthermore, the  $I_{pyro}(T)$  data given  $E_{pole} = \pm 10$  kV/cm are plotted in Fig. 9(d) and a complete  $P$  reversal is demonstrated by the sign-opposite but magnitude-identical two curves, as further concurred by the as-evaluated  $P(T)$  in Fig. 9(e), revealing the FIE characteristics. The negative–positive crossover occurs roughly at  $T \sim T_{P=0} \sim T_{Dy}$ , while this  $T_{P=0}$  may vary upon the different measuring conditions. More detailed analysis on the data can be found in earlier report.<sup>34</sup>

### 3.2. Model for ferrielectricity

Given the FIE characteristics, one is concerned with the underlying mechanism. Starting from the structural model shown in Fig. 4(b) for  $DyMn_2O_5$ , it is noted that the Dy spins are disordered until  $T_{N2}$  (or  $T_{N3}$ ), below which the Dy spin ordering proceeds. Therefore, the spin configuration in Fig. 4(b) represents the state below  $T_{N2}$  (or  $T_{N3}$ ). Without losing generality, we discuss the structural model in Fig. 4(b).

Consulting to the exchange striction scenario shown in Fig. 5 for  $RMn_2O_5$  with nonmagnetic R ion, one can easily propose a similar scenario for  $DyMn_2O_5$ , taking the  $Mn^{4+}$  ions as reference points. The spin lattice projected on the  $ab$ -plane is presented in Fig. 10(a), while the three-spin blocks to



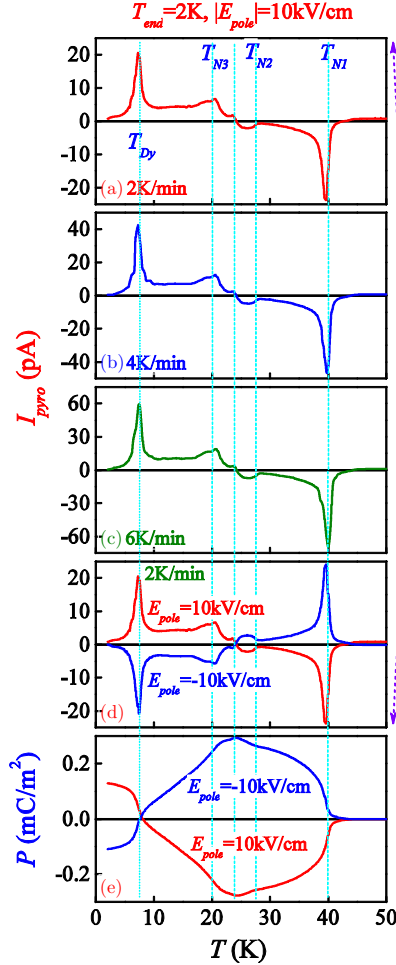


Fig. 9. (Color online) Measured pyroelectric current  $I_{\text{pyro}}(T)$  curves at warming rate of 2 K/min (a), 4 K/min (b), 6 K/min (c), respectively, using the Pyro method with  $E_{\text{pole}} = 10$  kV/cm. The  $I_{\text{pyro}}(T)$  curves at 2 K/min with  $E_{\text{pole}} = \pm 10$  kV/cm and the corresponding polarization  $P(T)$  curves are presented in (d) and (e), respectively.

be considered are plotted in Figs. 10(b) and 10(c), respectively. In spite of the non-negligible noncollinear components, the three spins in each block are roughly parallel or antiparallel along the  $b$ -axis. For the  $\text{Mn}^{3+}\text{--Mn}^{4+}\text{--Mn}^{3+}$  blocks, the two  $\text{Mn}^{3+}$  ions shift upward along the  $b$ -axis with respect to the central  $\text{Mn}^{4+}$  ion due to the exchange striction, leading to a local polarization  $P_{\text{MM}}$ . Contrary to this effect, the two  $\text{Dy}^{3+}$  ions in the  $\text{Dy}^{3+}\text{--Mn}^{4+}\text{--Dy}^{3+}$  blocks shift downward along the  $b$ -axis, leading to a local polarization  $P_{\text{DM}}$ . These blocks organize themselves by alternative stacking and occupy the whole  $ab$ -plane, constituting two FE sublattices  $P_{\text{MM}}$  and  $P_{\text{DM}}$ , to be discussed in detail below.

What should be reminded here is that various  $\text{RMn}_2\text{O}_5$  members may have different spin structures. For  $\text{GdMn}_2\text{O}_5$  and most members other than  $\text{DyMn}_2\text{O}_5$ , the Mn spins align majorly along the  $a$ -axis instead of the  $b$ -axis.<sup>48</sup> However, the exchange striction model remains similar and the  $P_{\text{MM}}$  still aligns along the  $b$ -axis. In addition, for  $\text{DyMn}_2\text{O}_5$  here, the

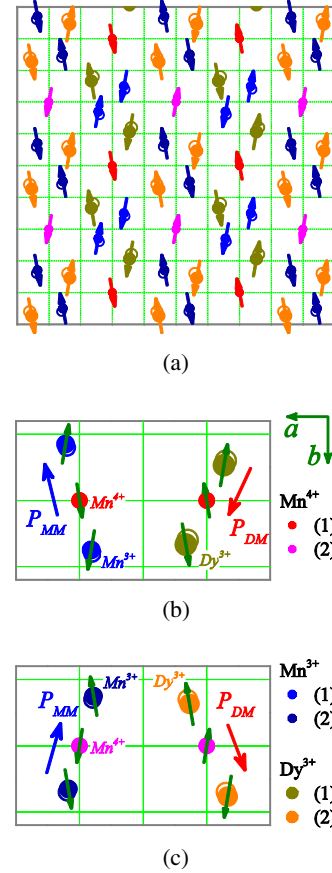


Fig. 10. (Color online) (a) Spin structure of  $\text{DyMn}_2\text{O}_5$  below  $T_{N2}$  ( $T_{N3}$ ) projected in the  $ab$  plane, where the solid (open) dots represent the ionic sites considering (ignoring) the exchange striction effect, with the  $\text{Mn}^{4+}$  ions as the reference positions. The four types of three-ion blocks are plotted in (b) and (c) with the exchange striction induced local electric polarizations  $P_{\text{MM}}$  and  $P_{\text{DM}}$ . The ionic sizes are shown only for guide of eyes.

$P_{\text{DM}}$  sublattice is not generated until  $T < T_{N2}$  (or  $T_{N3}$ ), implying that only the  $P_{\text{MM}}$  sublattice is available above  $T_{N2}$  (or  $T_{N3}$ ), which disappears at  $\sim T_{N1}$ .

We discuss the details of this ferroelectricity. Upon decreasing  $T$  from  $T_{N0}$ , the negative  $P$  appears at  $\sim T_{N1}$  and its magnitude increases rapidly, as shown in Fig. 11, curve (a), implying that the  $P_{\text{MM}}$  sublattice aligns in opposite to the poling field ( $E_{\text{pole}}$ ). The  $P_{\text{DM}}$  sublattice, opposite to the  $P_{\text{MM}}$  sublattice, enters at  $T \sim T_{N2}$  (or  $T_{N3}$ ) and the  $P_{\text{DM}}$  magnitude increases gradually until  $\sim T_{P=0}$  below which  $P_{\text{DM}} \geq |P_{\text{MM}}|$ , enabling the crossover from the  $P < 0$  to the  $P > 0$  (Fig. 11, curve (a)).

In addition, for those  $\text{RMn}_2\text{O}_5$  with nonmagnetic R, the magnetic ordering is far from complicated as that in  $\text{DyMn}_2\text{O}_5$ , implying that the latter is more or less related to the Dy–Mn coupling.<sup>43–48</sup> As the zero-order approximation, one may assume that the  $P_{\text{MM}}$  sublattice is irrelevant with the Dy–Mn coupling which is actually not true to some extent, and thus  $P_{\text{MM}}$  as a function of  $T$  reaches smoothly the

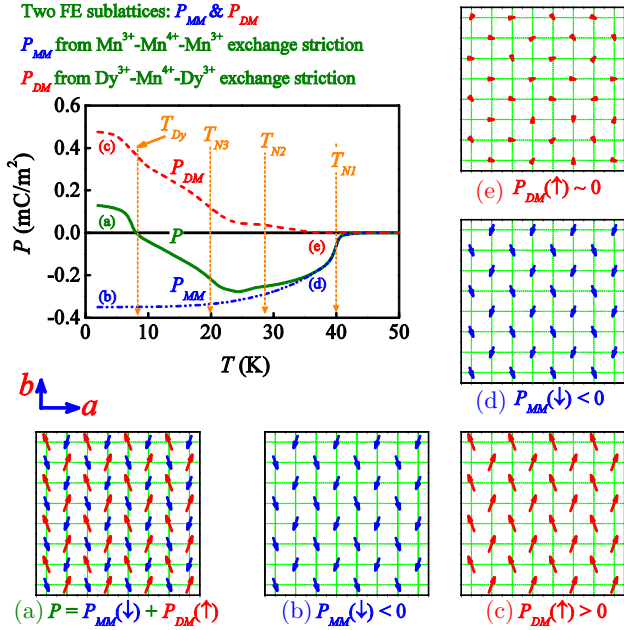


Fig. 11. (Color online) The proposed FIE lattice model for  $DyMn_2O_5$ . The measured  $P(T)$  curve as well as the speculative  $P_{MM}(T)$  and  $P_{DM}(T)$  curves are plotted together. The proposed FIE lattice,  $P_{DM}$  sublattices and  $P_{MM}$  sublattices at  $T < T_{Dy}$  and  $T < T_{N1}$  are plotted in (a)–(e), respectively, only for guide of eyes.

saturated value. This  $P_{MM}(T)$  dependence is shown in Fig. 11, curve (b) (dashed blue line). Consequently, the as-extracted  $P_{DM}(T)$  curve is plotted in Fig. 11, curve (c). The minor features at  $\sim T_{N2}$ ,  $T_{N3}$ , and  $T_{Dy}$ , are all due to the Dy–Mn coupling induced magnetic orderings. To this stage, the  $P_{MM}$  and  $P_{DM}$  as a function of  $T$  respectively are intentionally separated based on the several assumptions.

In correspondence to the  $P_{MM}(T)$  and  $P_{DM}(T)$  curves, the two FE sublattices below  $T_{Dy}$  and  $T_{N1}$  are schematically shown in Figs. 11(b), 11(c) and 11(d), 11(e), respectively, with the FIE lattice shown in Fig. 11(a). The observed  $P(T)$  dependence is reasonably explained by the proposed FIE model at least qualitatively, although it may be oversimplified and many details associated with the magnetic ordering are ignored, which is questionable but the FIE scenario remains unaffected.

### 3.3. Magnetoelectric effect

As mentioned in Sec. 2, the  $4f$  spin order in oxides is usually fragile against stimuli and the magnetic field driven re-orientation of  $4f$  spins can be realized at a field far lower than  $\sim 1.0$  T. In  $DyMn_2O_5$ , the Mn spin order is sufficiently high against magnetic field above  $\sim 10$  T.<sup>35–42</sup> In this case, one has reason to expect that the Dy spin order stability can be enhanced significantly by the Dy–Mn coupling, up to several Tesla. Therefore, the Dy spin re-orientation can be illustrated in Fig. 12(a), where an  $H//a$ -axis drives the Dy spins along the  $b$ -axis to re-orient and thus disables the exchange

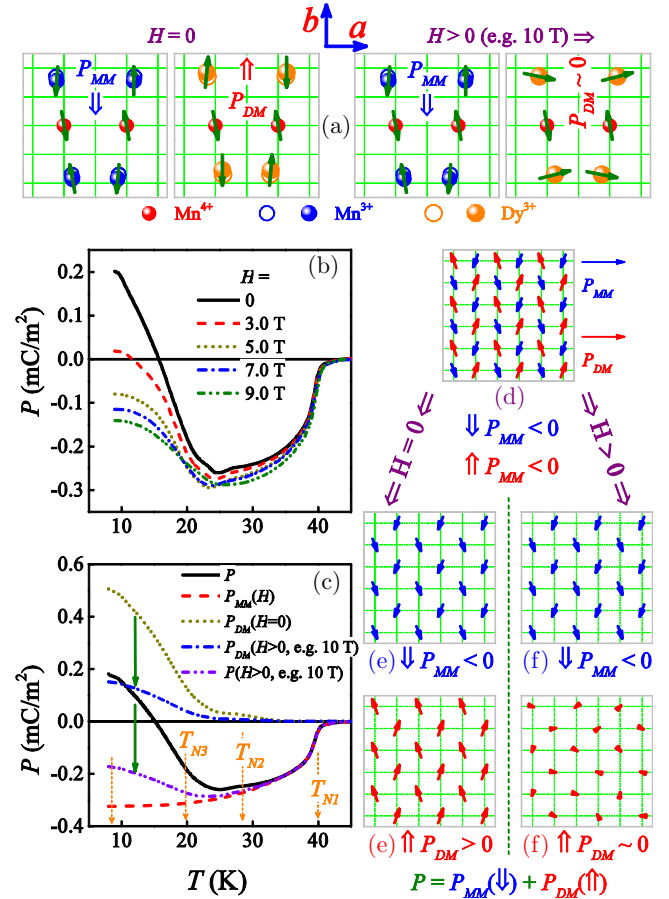


Fig. 12. (Color online) The proposed three-ion spin blocks under  $H = 0$  and  $H > 0$  (e.g., 10 T) are plotted in (a). The measured  $P(T)$  curves under various  $H$  are presented in (b). As an example, the  $P_{MM}(T)$  and  $P_{DM}(T)$  curves together with the  $P(T)$  curves under  $H = 0$  and  $H > 0$  (e.g., 10 T) are plotted in (c), where  $P_{MM}(T)$  is assumed to be robust against  $H$ . The FIE lattice is given in (d), and the corresponding two sublattices under  $H = 0$  and  $H > 0$  are shown in (e) and (f) for illustrating the consequence of applying magnetic field.

striction induced Dy ions' shift along the  $b$ -axis, i.e., melts away the  $P_{DM}$  sublattice, resulting in significant magnetoelectric effect.

Our experiments did confirm this prediction. The sample was first electrically poled down to  $T \sim 6$  K, and the poling was removed, followed by applying a given  $H$ . After the sample was sufficiently short-circuited, the pyroelectric current under the given  $H$  was collected during the warming process. The measured  $P(T)$  curves under a series of  $H$  are plotted in Fig. 12(b). The magnetic field does suppress the positive  $P$  in the low  $T$ -range, leading to the negative  $P$  over the whole  $T$ -range at  $H > 3.0$  T. This effect is qualitatively drawn in Fig. 12(c) where the vertical solid olive arrows indicate the  $H$ -induced suppression of  $P_{DM}$  and then  $P$ , while  $P_{MM}$  remains little suppressed. The responses of the two sublattices to  $H$  are schematically drawn in Figs. 12(d)–12(f).

### 3.4. Discussion

The proposed FIE model seems to reasonably explain all the observed phenomena associated with the unusual  $P(T)$  and  $P(H)$  dependences in  $\text{DyMn}_2\text{O}_5$ , although those features at  $T_{N2}$ ,  $T_{N3}$ , and  $T_{\text{Dy}}$  remains unclear yet. Nevertheless, additional more convincing evidence concurring with this model is required, since a connection of the polarization crossover at  $T_{P=0}$  with the FIE model is far from sufficient.

The magnetoelectric effect reported above suggests an alternative strategy. While the suppression of the collinear Dy spin order contributing to the  $P_{\text{DM}}$  can be realized by applying a magnetic field, it would be done too by nonmagnetic substitution of Dy, which can definitely inactivate the exchange striction in the  $\text{Dy}(\text{R})^{3+}\text{--Mn}^{4+}\text{--Dy}(\text{R})^{3+}$  blocks and thus remove gradually the  $P_{\text{DM}}$  sublattice with increasing substitution level. Stimulated by this approach, one can consider a nonmagnetic substitution of  $\text{Mn}^{3+}$  too, which can surely remove gradually the  $P_{\text{MM}}$  sublattice. Given a proper

design of the substitution experiments, one may reach a status in which one sublattice is gradually removed while the other remains less affected so that an FIE–FE transition is expected at certain substitution level. In addition, for the latter case, a critical issue is that the Mn-site substitution has to exclude the replacement of  $\text{Mn}^{4+}$  ions since the two sublattices would be removed simultaneously of the  $\text{Mn}^{4+}$  site is occupied with nonmagnetic ion.

The above discussion can be highlighted in Fig. 13, where the double-line arrows denote the  $P_{\text{MM}}$  and  $P_{\text{DM}}$ , respectively and their coarseness scales the magnitude. The exchange striction modes for  $P_{\text{MM}}$  and  $P_{\text{DM}}$  in  $\text{DyMn}_2\text{O}_5$  are shown in Fig. 13(a), while the consequences of nonmagnetic substitutions at  $\text{Mn}^{4+}$ -site,  $\text{Mn}^{3+}$ -site, and  $\text{Dy}^{3+}$ -site, respectively, are shown in Figs. 13(c)–13(e). The substitution at either  $\text{Mn}^{3+}$  site or  $\text{Dy}^{3+}$  site is clearly illustrated. For comparison, the consequence of imposing a magnetic field is re-given in Fig. 13(b). A realization of these roadmaps relies on several pre-requisites, while a reliable check of the FIE model will be questioned otherwise. First, the substitution should distort the lattice as weakly as possible so that the exchange interactions remain less perturbed. Second, the valence state should be maintained to avoid any charge doping. Third, the correct site occupation is critical since  $\text{DyMn}_2\text{O}_5$  is an occupation-ordered compound.

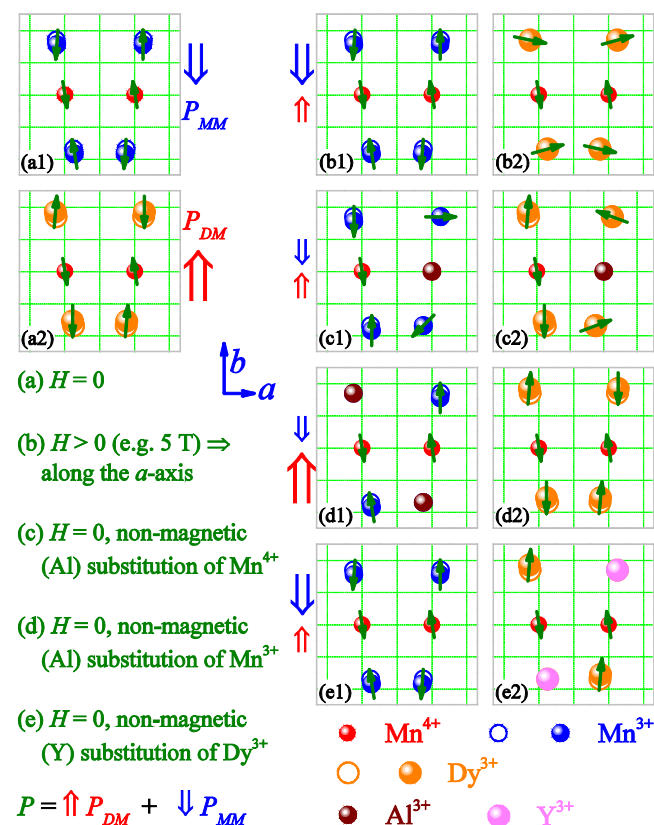


Fig. 13. (Color online) The proposed substitution strategy for  $\text{DyMn}_2\text{O}_5$ , as illustrated by the three-ion spin blocks. The solid (open) dots represent the ionic sites considering (ignoring) the exchange striction effect, with the  $\text{Mn}^{4+}$  ions as the reference positions. The spin structures in these blocks for (a)  $x = 0$  and  $H = 0$ , (b)  $x = 0$  and  $H > 0$  (e.g., 5–10 T), (c) Al substitution of  $\text{Mn}^{4+}$  and  $H = 0$ , (d) Al substitution of  $\text{Mn}^{3+}$  and  $H = 0$ , and (e) Y substitution of  $\text{Dy}^{3+}$  and  $H = 0$ , are schematically drawn, respectively. The blue  $\downarrow$  and red  $\uparrow$  arrows denote the  $P_{\text{MM}}$  and  $P_{\text{DM}}$  for these cases, with the coarseness representing the Magnitudes.

## 4. The Al Substitution of Mn: Proof Test I

### 4.1. Structural distortion, chemical valence states, and magnetism

As the one side of the evidence coin for the FIE model, the  $\text{Mn}^{3+}$ -site substitution by  $\text{Al}^{3+}$  is considered.<sup>49</sup> It is noted that  $\text{Al}^{3+}$  is only slightly smaller than  $\text{Mn}^{3+}/\text{Mn}^{4+}$  and the electronegativity values of Mn and Al are similar too. While details of the polycrystalline  $\text{DyMn}_{2-x}\text{Al}_x\text{O}_5$  sintering were described previously, we present in Fig. 14(a) the room temperature  $\theta - 2\theta$  X-ray diffraction patterns for a series of samples. All the reflections can be indexed by the standard database of  $\text{DyMn}_2\text{O}_5$ , and peak shifting towards the high-angle side is observed as seen in the insert of Fig. 14(b). Substitution up to  $x \sim 0.20$  does not change the lattice symmetry and induce any minor impurity phase. As an example, the Rietveld refining of the data for sample  $x \sim 0.04$  is as shown in Fig. 14(b), with the refining reliability as high as  $R_{\text{wp}} \sim 4.48\%$ .

The evaluated lattice unit volume  $V$  as a function of  $x$  plotted in Fig. 14(c) shows a linearly decreasing dependence consistent with the Vegard's law, implying the favored substitution of  $\text{Mn}^{3+}$  ions by  $\text{Al}^{3+}$  ions. Additional careful checking of the valence states of Mn using the XPS determination upon the substitution is performed, revealing no trace of intensity from  $\text{Mn}^{5+}$  or  $\text{Mn}^{2+}$  within the apparatus resolution. Since the binding energies for the  $\text{Mn}^{3+}2p_{1/2}/\text{Mn}^{4+}2p_{1/2}$  and  $\text{Mn}^{3+}2p_{3/2}/\text{Mn}^{4+}2p_{3/2}$  are close

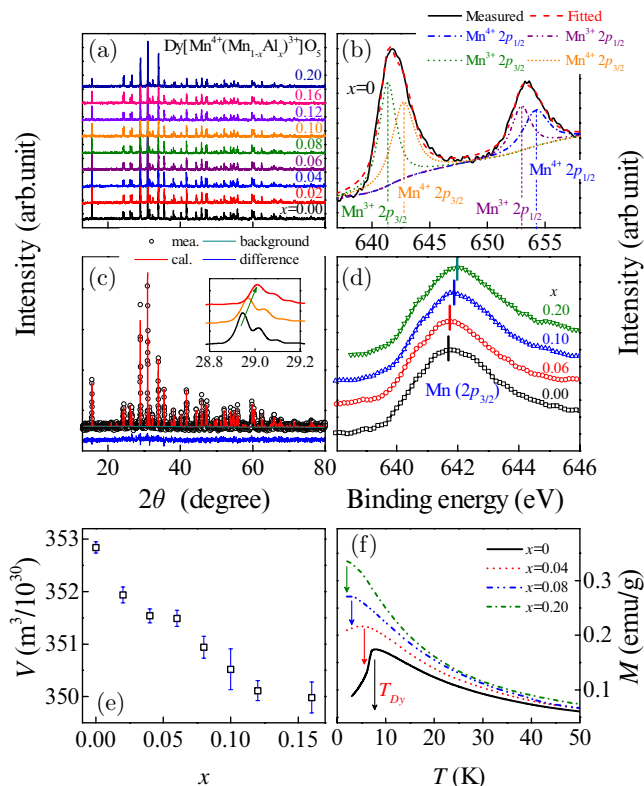


Fig. 14. (Color online) The consequences of Al substitution of Mn: (a) measured XRD  $\theta$ - $2\theta$  spectra for a series of  $\text{DyMn}_{2-x/2}\text{Al}_{x/2}\text{O}_5$  samples; (b) the Rietveld refined data for  $x = 0.04$  and the insert shows the local reflections of three samples  $x = 0.00$ ,  $0.10$ , and  $0.16$ ; (c) the fitted unit volume  $V$  as a function of  $x$  with uncertainties; (d) measured XPS spectrum for sample  $x = 0.0$  as an example, where the  $\text{Mn}^{3+}$  and  $\text{Mn}^{4+}$  core energy levels are labeled and the measured peaks are decomposed as the superimposition of the contributions from the  $\text{Mn}^{3+}$  and  $\text{Mn}^{4+}$  excitations, respectively; (e) the local peaks around  $642\text{ eV}$  corresponding to the  $\text{Mn}(2p_{3/2})$  core level. The peak shifting toward the high energy with increasing  $x$  is shown, indicating the increasing  $\text{Mn}^{4+}/\text{Mn}^{3+}$  ratio; (f) measured  $M$  for samples  $x = 0.00$ ,  $0.04$ ,  $0.08$ , and  $0.20$ , as a function of  $T$ , respectively.

to each other, a highly reliable fitting of the XPS peaks associated with Mn is required. Figure 14(d) shows this fitting for sample  $x = 0.0$ , and the  $\text{Mn}^{3+}/\text{Mn}^{4+} \sim 1.0$  is suggested by comparing the shadow area below peaks  $\text{Mn}^{3+}2p_{1/3}$  and  $\text{Mn}^{3+}2p_{3/2}$  with that below peaks  $\text{Mn}^{4+}2p_{1/3}$  and  $\text{Mn}^{4+}2p_{3/2}$ . The same fitting procedure is applied to other samples and the fitted  $\text{Mn}^{3+}/\text{Mn}^{4+}$  ratios are consistent with the nominal ones with an uncertainty of  $\sim 10\%$ , suggesting that the  $\text{Al}^{3+}$  ions do occupy the  $\text{Mn}^{3+}$  sites rather than the  $\text{Mn}^{4+}$  ones. The amplified  $\text{Mn}(2p_{3/2})$  peaks for several samples are summarized in Fig. 14(e). The gradual peak shifting towards the high-energy side with increasing  $x$  is concededly identified, indicating more  $\text{Mn}^{4+}$  ions than  $\text{Mn}^{3+}$  ions in samples with higher  $x$  and confirming again that the  $\text{Al}^{3+}$  ions substitute the  $\text{Mn}^{3+}$  ions rather than  $\text{Mn}^{4+}$  ions.<sup>49</sup>

Although the possibility for minor occupation of the  $\text{Mn}^{4+}$  sites by  $\text{Al}^{3+}$  for higher  $x$  cases cannot be excluded, the  $\text{Al}^{3+}$ -occupation of  $\text{Mn}^{3+}$  is dominant. By the way, the magnetization response to the substitution can be used to measure the impact on the Dy–Dy exchange interaction, as shown in Fig. 4(f) for several samples. The  $T_{\text{Dy}}$  is remarkably suppressed with increasing  $x$  down to  $\sim 2\text{ K}$  at  $x = 0.20$ .

#### 4.2. Suppression of $P_{\text{MM}}$ sublattice and polarization reversal

The measured  $I_{\text{pyro}}(T)$  and  $P(T)$  curves for a series of samples are presented in Figs. 15(a)–15(g), with the  $I_{\text{pyro}}(T)$  curve for  $x = 0.0$  in each plot for comparison. The Al-substitution leads to several interesting features. First, the negative  $I_{\text{pyro}}$  peak right below  $T_{N1}$  is suppressed and downshifted with increasing  $x$ , indicating the suppression of  $P_{\text{MM}}$ , suggesting the damage of the exchange striction of the  $\text{Mn}^{3+}\text{--Mn}^{4+}\text{--Mn}^{3+}$  blocks. Second, the positive  $I_{\text{pyro}}$  peak around  $T_{\text{Dy}}$  at  $x = 0.0$  indicated by the arrow in Fig. 15(a) becomes weak at  $x = 0.02$  and disappears at  $x = 0.04$  and higher. Third, the broad current bump around  $T_{N3}$  at  $x = 0.0$  is evolved into a sharp peak locating in-between  $T_{N2}$  and  $T_{N3}$  for low  $x$  ( $x < 0.08$ ), increasing in height and shifting rightward, in contrast to the variations of the negative peak right below  $\sim T_{N1}$ . Eventually, the two peaks meet and annihilate with each other. The last ‘moment’ of the two peak

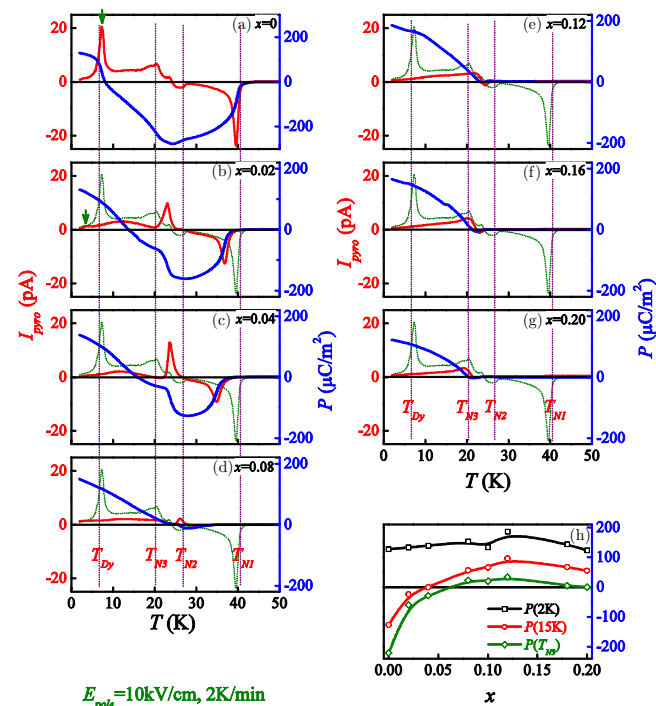


Fig. 15. (Color online) Measured pyroelectric current  $I_{\text{pyro}}(T)$  and evaluated polarization  $P(T)$  for a series of samples in (a)–(g), where the  $I_{\text{pyro}}(T)$  data for sample  $x = 0.0$  are inserted for reference. The  $P$  data at several  $T$  as a function of  $x$  are plotted in (h).



annihilation is at  $x \sim 0.08$ . The two peaks correspond respectively to the polarization generation at the higher- $T$  side and disappearance at the lower- $T$  side, and their simultaneous evolutions illustrates how  $P_{MM}$  is suppressed upon the substitution.

The Al-substitution certainly damages the  $P_{DM}$  too because the spin structure is gradually diluted. The measured  $P$  ( $=|P_{DM}| - |P_{MM}|$ ) in the low- $T$  range does not show substantial increase with the gradual suppression of  $P_{MM}$ , implying the deterioration of  $P_{DM}$  with increasing  $x$ . Nevertheless,  $P_{DM}$  is more robust than  $P_{MM}$  against the substitution, suggesting that the Al-substitution does not change much the Dy<sup>3+</sup>–Mn<sup>4+</sup> coupling. Furthermore, the Al-substitution induced suppression of  $P_{MM}$  certainly leads to a negative–positive crossover of  $P$ , illustrated by the  $P(x)$  curves in Fig. 15(h). Reasonably, the  $P(x)$  at  $T \sim 2$  K is always positive due to  $|P_{DM}| > |P_{MM}|$  but the  $P(x)$  curves at both  $T \sim 15$  K and  $\sim T_{N3}$  change their signs at certain  $x$  ( $x \sim 0.04$  and  $0.065$ ).

## 5. The Y Substitution of Dy: Proof Test II

As the other side of the evidence coin for the FIE model, the Y<sup>3+</sup>-substitution of Dy<sup>3+</sup> is a proper approach.<sup>50</sup> The Y<sup>3+</sup> ionic radius ( $\sim 0.090$  nm) is slightly smaller than Dy<sup>3+</sup> ( $\sim 0.091$  nm), and the Y substitution allows the induced lattice distortion as small as possible. Nevertheless, the Dy–Mn coupling and Dy–Dy interactions can be substantially manipulated by the substitution, and the direct consequence is gradual suppression of the  $P_{DM}$  sublattice but the  $P_{MM}$  sublattice remains less perturbed.

### 5.1. Structural, specific heat, and magnetization

The crystallinity and lattice distortion for several samples were checked by the XRD  $\theta$ - $2\theta$  spectra in Fig. 16(a). The substitution up to  $x \sim 0.20$  does not change the lattice symmetry and all the reflections can be indexed. The gradual peak shifting with increasing  $x$  is shown in the inset of Fig. 16(c), with the data refinement for sample  $x = 0.10$  shown in Fig. 16(b). The evaluated unit lattice volume  $V$  as a function of  $x$  is presented in Fig. 16(c), following the Vegard's law, suggesting the Y substitution of Dy rather than Mn.

The specific heat  $C_P(T)$  and magnetization  $M(T)$  data are presented in Fig. 16(d). For  $x = 0$ , the  $C_P(T)$  data feature the spin orderings at  $T_{N1}$ ,  $T_{N2}$ ,  $T_{N3}$ , and  $T_{Dy}$ , respectively. The positions of  $T_{N1}$  and  $T_{N2}$  do not depend on  $x$ , but the transition at  $T_{N3}$  becomes vague and the  $T_{Dy}$  is down-shifted remarkably, suggesting the instability of the Dy spin order and the weakened Dy–Mn coupling, obviously due to the Dy network dilution by the substitution. The  $M(T)$  curves for these samples are plotted in Fig. 16(e), and again no identifiable spin ordering features can be observed except the shifting of the broad peak at  $T_{Dy}$  associated with the Dy spin ordering. A substitution up to  $x = 0.20$  does not yet collapse

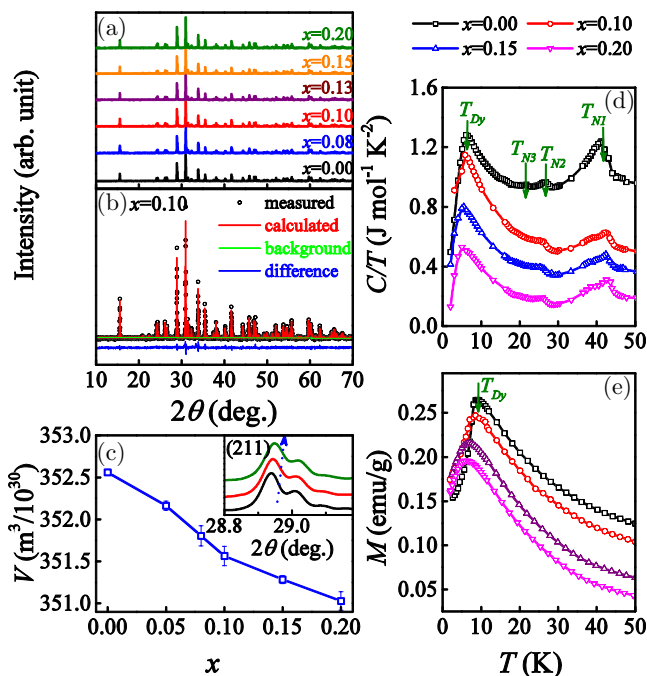


Fig. 16. (Color online) The consequences of Al substitution of Mn: (a) measured XRD  $\theta$ - $2\theta$  spectra for a series of samples; (b) the Rietveld refined data for sample  $x = 0.10$ ; (c) the fitted unit volume  $V$  as a function of  $x$ , and the insert shows the local reflections around  $2\theta \sim 29^\circ$  for samples  $x = 0, 0.10$ , and  $0.20$ ; (d) measured specific heat  $C_P/T$  and (e) measured  $M$  for several samples, as a function of  $T$ , respectively.

the Dy spin ordering, implying that the Dy–Mn coupling in  $\text{DyMn}_2\text{O}_5$  is strong enough. However, the  $P_{DM}$  sublattice will most likely be destabilized in prior to the disordering of the Dy spins, since the ferroelectricity is anyhow a second-order effect with respect to the spin order and the inter-dipole interactions must be much weaker than the exchange interactions.

### 5.2. Modulation of electric polarization

The measured  $P(T)$  (blue curves) and  $I_{\text{pyro}}(T)$  (red curves) for several samples are plotted in Figs. 17(a) to 17(f), respectively,<sup>50</sup> with several clear features in terms of ferroelectricity. First, the sharp  $I_{\text{pyro}}$  peaks at  $\sim T_{Dy}$  and  $\sim T_{N1}$  for  $x = 0$  become gradually suppressed as  $x > 0.05$  until  $x = x_c \sim 0.13$  where the peak reversal occurs, signing the polarization reversal. Second, the magnitude of  $P$  over the whole  $T$ -range decays gradually until  $x = x_c \sim 0.13$ , and then increases gradually. At  $x \sim 0.15$  and  $\sim 0.20$ , the  $P(T)$  data no longer exhibit the FIE-like behavior but more FE-like, regardless the anomalous features around  $T_{N3}$ . The substitution induced  $P$  reversal can be more clearly identified by plotting the  $P(x)$  data at several  $T$ , as shown in Fig. 17(g). The reversal at  $T \sim 15$  K and  $T_{N3}$  occurs round  $x_c \sim 0.13$ , while the  $P(x)$  at  $T \sim 2$  K, which is always positive, exhibits a valley around  $x_c \sim 0.13$  too.

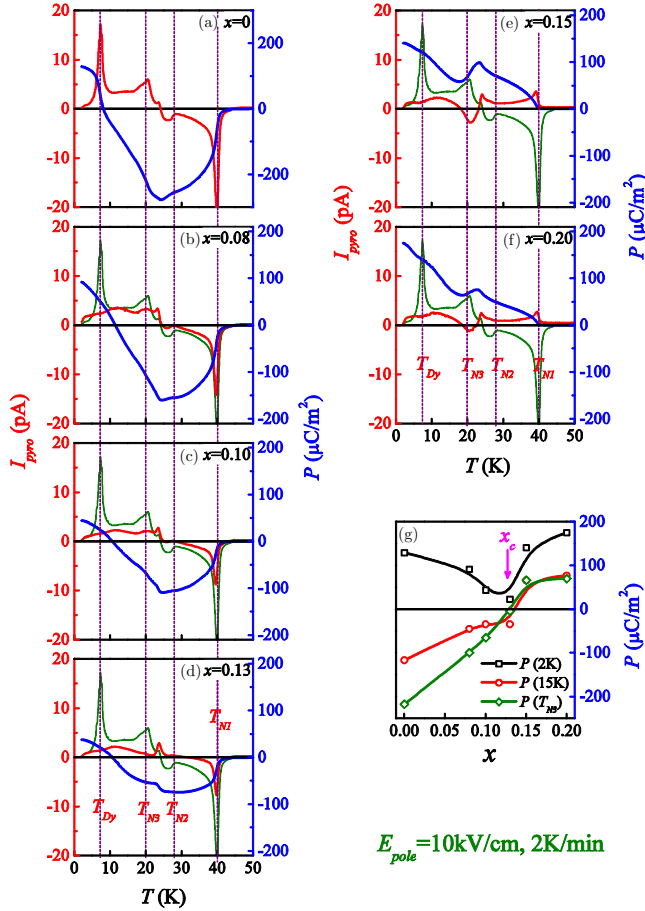


Fig. 17. (Color online) Measured pyroelectric current  $I_{\text{pyro}}(T)$  and evaluated polarization  $P(T)$  for a series of samples (a)–(f), where the  $I_{\text{pyro}}(T)$  data for sample  $x = 0$  are inserted for reference. The  $P$  data at several  $T$  as a function of  $x$  are plotted in (g).

### 5.3. Domain model for polarization modulation

The  $P(T, x)$  data presented above do show substantial variations upon the Y substitution, including the polarization reversal around  $x_c$ . However, a connection between the observed behaviors and the proposed FIE model is not straightforward, appealing for a bridge of the polarization reversal with the sublattice instability. It is noted that all the samples were electrically pre-poled down to  $T_{\text{end}} \sim 2 \text{ K}$  in prior to the pyroelectric current collection. This implies that the  $P_{DM}$  sublattice aligns along  $E_{\text{pole}}$  (upward), opposite to the  $P_{MM}$  sublattice. Nevertheless, the two sublattices each consist of mesoscopic domains, i.e., the  $P_{DM}$ -domains and  $P_{MM}$ -domains. The whole FIE lattice contains overlapped  $P_{DM}$ -domains and  $P_{MM}$ -domains which are inter-coupled and antiparallel. The random Y-substitution allows those  $P_{DM}$ -domains with higher Y concentration to be unstable and replaced by PE phase, while the  $P_{MM}$ -domains remain less perturbed. Here two specific temperatures are chosen for illustrating the domain evolutions associated with the polarization modulation.

First, at a low- $T$  ( $\sim T_{Dy}$ ) where  $P = P_{DM} + P_{MM} > 0$  (Fig. 18).<sup>50</sup> Each domain is denoted by one square dot, and the aligned squares constitute the  $P_{DM}$  sublattice (top row) and  $P_{MM}$  sublattice (bottom row). The Y substitution damages some  $P_{DM}$  domains so that the local  $P_{DM} = 0$  (white squares) while the  $P_{MM}$ -domains may be reversed by  $E_{\text{pole}}$ , as labeled by the orange squares, and thus the local  $P_{MM} > 0$ . The averaged  $P_{DM}$  and  $P_{MM}$  over the whole lattice decrease slightly with increasing  $x$ . At  $x \sim x_c$ , all the  $P_{MM}$ -domains with  $P_{MM} < 0$  are reversed by  $E_{\text{pole}}$  and those  $P_{DM}$ -domains will be reversed too to follow the antiparallel alignment with the corresponding  $P_{MM}$ -domains, due to the ferroelectricity nature. In consequence, the  $P(x)$  remains positive but a minimal will appear at  $\sim x_c$ . The whole sequence is schematically drawn in Figs. 18(a)–18(e), consistent with the measured  $P(x)$  data at  $T \sim 2 \text{ K}$  in Fig. 18(g).

Similar analysis can be applied to the cases at higher  $T$  where  $P$  is negative. At this temperature, sample  $x = 0$  offers  $|P_{DM}| \ll |P_{MM}|$  although  $|P_{DM}| > |P_{MM}|$  at low  $T$ . The  $P_{DM}(T)$  will decay more rapidly than the  $P_{MM}(T)$  and eventually becomes disappeared respectively at  $\sim T_{N3}$  and  $\sim T_{N1}$ . Since

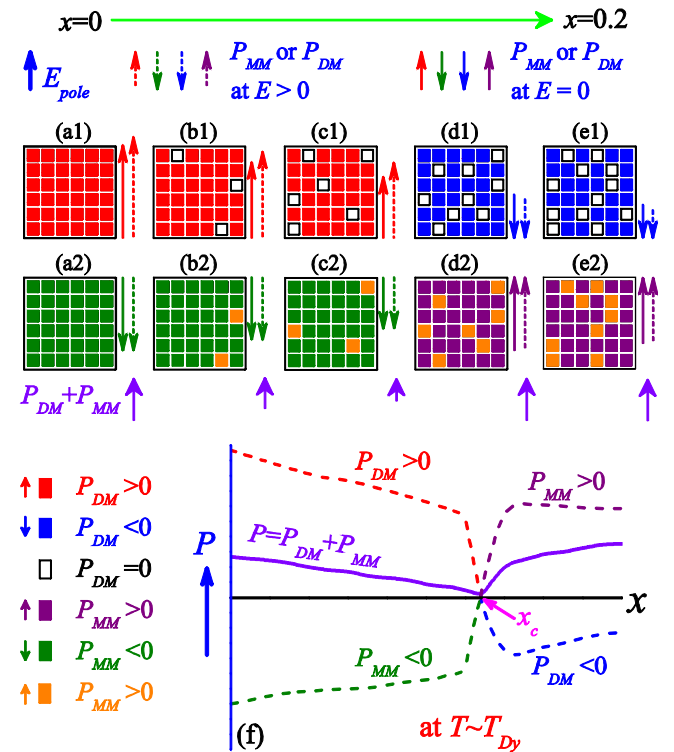


Fig. 18. (Color online) Schematic drawing of domain structure evolution of the  $P_{DM}$  sublattice (top row) with the  $P_{DM}$ -domains (square dots) and  $P_{MM}$  sublattice (bottom row) with the  $P_{MM}$ -domains (square dots) in the FIE domain structure for a series of samples from  $x = 0.00$  to  $x \sim 0.20$ , at low  $T(\sim T_{Dy})$ . The solid and dashed arrows aside each sublattice represent the polarizations  $P_{DM}$  and  $P_{MM}$  of the two sublattices under electric field  $E = 0$  and  $E > 0$ , respectively. The proposed  $P_{DM}$  and  $P_{MM}$ , and the measured  $P$ , as a function of  $x$ , are plotted in (f) for the guide of eyes.

the samples were pre-poled down to the lowest  $T$  ( $\sim 2$  K), the  $P_{DM}$ -domains (red squares) still align along  $E_{\text{pole}}$  at  $x = 0$ . In this case, the evolution of the domain structure with  $x$  is similar to the low- $T$  cases described above, but the  $P(x)$  curve reverses its sign at  $\sim x_c$ . This explains reasonably the observed crossover of the  $P(T)$  curves at  $T \sim 15$  K and  $\sim T_{N3}$ , as shown in Fig. 17(g).

## 6. Conclusion and Perspectives

### 6.1. Conclusion

Motivated by the introduction in Sec. 1, possible ferrielectricity in  $\text{DyMn}_2\text{O}_5$  has been thoroughly discussed in Sec. 2 and then demonstrated by a series of experiments in the framework of the FIE lattice consisting of two FE sublattices in Secs. 3–5, respectively. To the end stage of this mini-review, we can reach the following points of conclusion.<sup>34,49,50</sup>

- (1) The clear sign-reversal of polarization as a function of  $T$  has been confirmed by highly reliable pyroelectric current data probed using the Pyro method. Along this line, an FIE behavior of  $\text{DyMn}_2\text{O}_5$  has been identified.
- (2) Based on available data on the lattice and spin structures of  $\text{DyMn}_2\text{O}_5$ , an FIE model has been proposed, which consists of two antiparallel FE sublattices. One sublattice is composed of ordered local  $P_{MM}$  generated from the  $\text{Mn}^{3+}\text{--Mn}^{4+}\text{--Mn}^{3+}$  blocks with the major  $\uparrow\uparrow\downarrow$  spin components along the  $b$ -axis or  $a$ -axis, and the other is occupied with ordered local  $P_{DM}$  generated from the  $\text{Dy}^{3+}\text{--Mn}^{4+}\text{--Dy}^{3+}$  blocks with the major  $\uparrow\uparrow\downarrow$  spin components along the  $b$ -axis or  $a$ -axis. Both sublattices are generated via the exchange striction mechanism and their total polarizations are aligned along the  $b$ -axis.
- (3) The FIE lattice model has been confirmed by the nonmagnetic substitution of  $\text{Mn}^{3+}$  by  $\text{Al}^{3+}$ , which suppresses gradually the  $P_{MM}$  sublattice and thus drives the polarization reversal at certain substitution level.
- (4) The nonmagnetic  $\text{Y}^{3+}$  substitution of  $\text{Dy}^{3+}$  has been performed also to check the FIE lattice model, which dilutes gradually the  $P_{DM}$  sublattice. This dilution also enables the reversal of the  $P_{MM}$  domains and thus a polarization reversal at certain substitution level has been revealed too.

The conclusion is ended with the two FE phase diagrams on the  $(x, T)$  plane for the  $\text{Mn}^{3+}$ -site substitution and  $\text{Dy}^{3+}$ -site substitution, as shown in Figs. 19(a) and 19(b), respectively. One can see that the phase plane for both cases can be divided into four regions: the PE region and regions I, II, and III. The major characters in terms of polarizations  $P_{MM}$ ,  $P_{DM}$ , and  $P = P_{MM} + P_{DM}$ , are clearly marked in these regions, not needing any additional description. One may address that such a polarization reversal in multiferroics with magnetically induced ferroelectricity has rarely been observed so far and

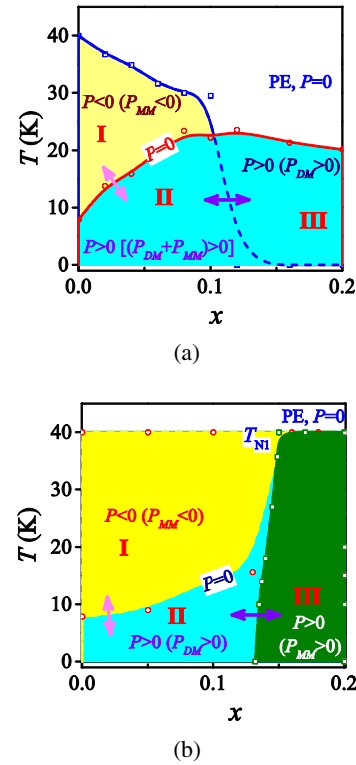


Fig. 19. (Color online) Evaluated ferroelectric phase diagrams on the  $(x, T)$  plane for the Al-substitution of Mn (a) and Y substitution of Dy (b). The whole phase plane are divided into four regions for each case, and the properties of the two sublattices  $P_{DM}$  and  $P_{MM}$  are labeled, while the polarization reversals are indicated by the solid double head arrows.

this is the first experimental evidence for the polarization reversal by chemical substitution.

### 6.2. Perspectives

The complexity of multiferroic physics in  $\text{DyMn}_2\text{O}_5$ , which accommodates both  $4f$  spins and  $3d$  spins, has been demonstrated in this work in addition to earlier reports.<sup>35–42</sup> We present a simple framework for this physics in terms of ferrielectricity, which allows opportunities for any potential manipulations of FE polarization in  $\text{RMn}_2\text{O}_5$ . Nevertheless, at least several major issues remain not yet well touched so far and some of them closely related to the present work can be outlined:

- (1) The contribution of the noncollinear components of Mn and Dy spins, if any, is entirely out of consideration in the present model. This contribution remains to be a debated issue for long time.
- (2) The spin structure variations and magnetic transitions around  $T_{N2}$ ,  $T_{N3}$ , and  $T_{Dy}$  are not well understood and in fact entirely ignored in the FIE lattice model here. All of our discussions start from the lattice and spin structures shown in Figs. 4 and 10, but these structures may not be applicable above  $T_{N2}$  ( $T_{N3}$ ). Uncertainties in terms of the

spin structure and microscopic mechanism for ferroelectricity cannot be excluded.

- (3) The role of the Dy–Dy ( $4f$ – $4f$ ) interaction has not yet been clearly identified in the present work, which may be non-negligible with respect to the Dy–Mn and Mn–Mn interactions. Usually, independent Dy spin ordering due to the Dy–Dy interaction is possible in spite of appearance at extremely low  $T$ . This effect is not considered in the present work.

Even though, it should be mentioned that the proposed ferrielectric model and the simple substitution strategy in this work enable our understanding of the physics of multiferroicity in a quite simplified framework. This framework seems to grasp the core of the physics. Its significance may be embarrassed from several aspects highlighted below:

- (1) The  $\text{RMn}_2\text{O}_5$  members with  $\text{R}=\text{Gd}$ ,  $\text{Tb}$ ,  $\text{Ho}$ , and  $\text{Er}$ , have similar spin structure as  $\text{DyMn}_2\text{O}_5$ . The present model would be of generality to some extent and can be used to explain most of the multiferroic behaviors observed in these materials.
- (2) Some additional ingredients of physics should be taken into account. First, the  $\text{R}$  ionic size variation is critical for the lattice distortion and thus the delicate balance of the multifold interactions. Second, the  $4f$ – $3d$  coupling between  $\text{R}$  and  $\text{Mn}$  ions is different for different members. The  $\text{Gd}$ – $\text{Mn}$ ,  $\text{Dy}$ – $\text{Mn}$ , and  $\text{Ho}$ – $\text{Mn}$  couplings are strong while the  $\text{Tb}$ – $\text{Mn}$  and  $\text{Er}$ – $\text{Mn}$  couplings are relatively weak. For the latter cases, the polarization arisen from the  $\text{R}$ – $\text{Mn}$  coupling may be small and thus the underlying physics becomes different.
- (3) Possible application of ferrielectricity can be recognized. Usually, ferrielectricity represents a property much less favorable than ferroelectricity for practical applications. Nevertheless, the present work suggests that a proper chemical substitution may make a ferrielectricity–ferroelectricity transition possible. In other words, by a critical substitution, the FE states as low-energy excitations of the FIE ground states may be reached, triggering possible multi-state memories applications. A similar example in  $\text{BaFe}_2\text{Se}_3$  was recently reported,<sup>70</sup> where two FIE states and two slightly metastable FE states can be easily inter-switched.

Finally but not the least, one is reminded of a recent work on ferroelectricity in  $\text{RMn}_2\text{O}_5$ , which claims the room temperature ferroelectricity associated with the lattice symmetry breaking.<sup>71</sup> The magnetically induced polarization below  $T_{\text{N1}}$  does add a component to the existing polarization. This issue, critical if true, deserves for critical checking.

## Acknowledgments

All the reported experimental data in this mini-review were measured and processed by Z. Y. Zhao. Fruitful discussions

with M. F. Liu and Z. B. Yan are appreciated. Partial results covered here have been published or under consideration in refereed journals (e.g., Ref. 50). This work was supported by the Natural Science Foundation of China (Grant Nos. 11234005 and 51431006) and the National 973 Projects of China (Grant No. 2011CB922101).

## References

- <sup>1</sup>S. W. Cheong and M. Mostovoy, Multiferroics: A magnetic twist for ferroelectricity, *Nat. Mater.* **6**, 13 (2007).
- <sup>2</sup>W. Eerenstein, N. D. Mathur and J. F. Scott, Multiferroic and magnetoelectric materials, *Nature* **442**, 750 (2006).
- <sup>3</sup>K. F. Wang, J.-M. Liu and Z. F. Ren, Multiferroicity: The coupling between magnetic and ferroelectric orders, *Adv. Phys.* **58**, 321 (2009).
- <sup>4</sup>S. Dong and J.-M. Liu, Recent progress of multiferroic perovskite manganites, *Mod. Phys. Lett. B* **26**, 1230004 (2012).
- <sup>5</sup>T. Kimura, T. Goto, H. Shintani, K. Ishizaka, T. Arima and Y. Tokura, Magnetic control of ferroelectric polarization, *Nature* **426**, 55 (2003).
- <sup>6</sup>N. Hur, S. Park, P. A. Sharma, J. S. Ahn, S. Guha and S. W. Cheong, Electric polarization reversal and memory in a multiferroic material induced by magnetic fields, *Nature* **429**, 392 (2004).
- <sup>7</sup>D. I. Khomskii, Multiferroics: Different ways to combine magnetism and ferroelectricity, *J. Magn. Magn. Mater.* **306**, 1 (2006).
- <sup>8</sup>H. Katsura, N. Nagaosa and A. V. Balatsky, Spin current and magnetoelectric effect in noncollinear magnets, *Phys. Rev. Lett.* **95**, 057205 (2005); I. A. Sergienko and E. Dagotto, Role of the Dzyaloshinskii-Moriya interaction in multiferroic perovskites, *Phys. Rev. B* **73**, 094434 (2006).
- <sup>9</sup>M. Mostovoy, Ferroelectricity in spiral magnets, *Phys. Rev. Lett.* **96**, 067601 (2006).
- <sup>10</sup>Y. Tokura and S. Seki, Multiferroics with spiral spin orders, *Adv. Mater.* **22**, 1554 (2010).
- <sup>11</sup>I. A. Sergienko, C. Sen and E. Dagotto, Ferroelectricity in the magnetic E-phase of orthorhombic perovskites, *Phys. Rev. Lett.* **97**, 227204 (2006).
- <sup>12</sup>T. Kimura, Magnetoelectric hexaferrites, *Ann. Rev. Condens. Matter Phys.* **3**, 93 (2012).
- <sup>13</sup>M. Biles and A. Barthelemy, Multiferroics: Towards a magnetoelectric memory, *Nat. Mater.* **7**, 425 (2008).
- <sup>14</sup>T. Arima, A. Tokunaga, T. Goto, H. Kimura, Y. Noda and Y. Tokura, Collinear to spiral spin transformation without changing the modulation wavelength upon ferroelectric transition in  $\text{Tb}_{1-x}\text{Dy}_x\text{MnO}_3$ , *Phys. Rev. Lett.* **96**, 097202 (2006).
- <sup>15</sup>H. Murakawa, Y. Onose, S. Miyahara, N. Furukawa and Y. Tokura, Ferroelectricity induced by spin-dependent metal-ligand hybridization in  $\text{Ba}_2\text{CoGe}_2\text{O}_7$ , *Phys. Rev. Lett.* **105**, 137202 (2010).
- <sup>16</sup>H. J. Xiang, E. J. Kan, Y. Zhang, M.-H. Whangbo and X. G. Gong, General theory for the ferroelectric polarization induced by spin-spiral order, *Phys. Rev. Lett.* **107**, 157202 (2011).
- <sup>17</sup>X. Z. Lu, M. H. Whangbo, S. Dong, X. G. Gong and H. J. Xiang, Giant ferroelectric polarization of  $\text{CaMn}_7\text{O}_{12}$  induced by a combined effect of Dzyaloshinskii-Moriya interaction and exchange striction, *Phys. Rev. Lett.* **108**, 187204 (2012).



- <sup>18</sup>J.-M. Liu and C. W. Nan, Decade of multiferroic researches, *Wuli* **43**, 88 (2014) (in Chinese).
- <sup>19</sup>Y. J. Choi, H. T. Yi, S. Lee, Q. Huang, V. Kiryukhin and S.-W. Cheong, Ferroelectricity in an Ising chain magnet, *Phys. Rev. Lett.* **100**, 047601 (2008).
- <sup>20</sup>J. Hemberger, F. Schrettle, A. Pimenov, P. Lunkenheimer, V. Yu. Ivanov, A. A. Mukhin, A. M. Balbashov and A. Loidl, Multiferroic phases of  $\text{Eu}_{1-x}\text{Y}_x\text{MnO}_3$ , *Phys. Rev. B* **75**, 035118 (2007).
- <sup>21</sup>S. Ishiwata, Y. Kaneko, Y. Tokunaga, Y. Taguchi, T. Arima and Y. Tokura, Perovskite manganites hosting versatile multiferroic phases with symmetric and antisymmetric exchange strictions, *Phys. Rev. B* **81**, 100411 (2010).
- <sup>22</sup>O. Prokhnenko, R. Feyerherm, E. Dudzik, S. Landsgesell, N. Aliouane, L. C. Chapon and D. N. Argyriou, Enhanced ferroelectric polarization by induced Dy spin order in multiferroic  $\text{DyMnO}_3$ , *Phys. Rev. Lett.* **98**, 057206 (2007).
- <sup>23</sup>R. Feyerherm, E. Dudzik, A. U. B. Wolter, S. Valencia, O. Prokhnenko, A. Maljuk, S. Landsgesell, N. Aliouane, L. Bouchemine, S. Brown and D. N. Argyriou, Magnetic-field induced effects on the electric polarization in  $\text{RMnO}_3$  ( $\text{R}=\text{Dy}, \text{Gd}$ ), *Phys. Rev. B* **79**, 134426 (2009).
- <sup>24</sup>J. Stremper, B. Bohnenbuck, M. Mostovoy, N. Aliouane, D. N. Argyriou, F. Schrettle, J. Hemberger, A. Krimmel and M. V. Zimmermann, Absence of commensurate ordering at the polarization flop transition in multiferroic  $\text{DyMnO}_3$ , *Phys. Rev. B* **75**, 212402 (2007).
- <sup>25</sup>N. Taira, M. Wakeshima and Y. Hinatsu, Magnetic susceptibility and specific heat studies on heavy rare earth ruthenate pyrochlores  $\text{R}_2\text{Ru}_2\text{O}_7$  ( $\text{R}=\text{Gd}-\text{Yb}$ ), *J. Mater. Chem.* **12**, 1475 (2002).
- <sup>26</sup>J. S. Gardner, M. J. P. Gingras and J. E. Greedan, Magnetic pyrochlore oxides, *Rev. Mod. Phys.* **82**, 53 (2010).
- <sup>27</sup>N. Zhang, Y. Y. Guo, L. Lin, S. Dong, Z. B. Yan, X. G. Li and J.-M. Liu, Ho substitution suppresses collinear Dy spin order and enhances polarization in  $\text{DyMnO}_3$ , *Appl. Phys. Lett.* **99**, 102509 (2011).
- <sup>28</sup>N. Zhang, S. Dong, G. Q. Zhang, L. Lin, Y. Y. Guo, J.-M. Liu and Z. F. Ren, Multiferroic phase diagram of Y partially substituted  $\text{Dy}_{1-x}\text{Y}_x\text{MnO}_3$ , *Appl. Phys. Lett.* **98**, 012510 (2011).
- <sup>29</sup>N. Zhang, S. Dong and J.-M. Liu, Ferroelectricity generated by spin-orbit and spin-lattice couplings in multiferroic  $\text{DyMnO}_3$ , *Front. Phys.* **7**, 408 (2012).
- <sup>30</sup>C. F. Pulvari, Ferroelectricity, *Phys. Rev.* **120**, 1670 (1960).
- <sup>31</sup>K. Rabe, Ch. H. Ahn and J. M. Triscone (eds.), *Physics of Ferroelectrics: A Modern Perspective* (Topics in Applied Physics, Springer-Verlag, Berlin, 2007).
- <sup>32</sup>N. Hur, S. Park, P. A. Sharma, S. Guha and S. W. Cheong, Colossal magnetodielectric effects in  $\text{DyMn}_2\text{O}_5$ , *Phys. Rev. Lett.* **93**, 107207 (2004).
- <sup>33</sup>M. Fukunaga and Y. Noda, Classification and interpretation of the polarization of multiferroic  $\text{RMn}_2\text{O}_5$ , *J. Phys. Soc. Jpn.* **79**, 054705 (2010).
- <sup>34</sup>Z. Y. Zhao, M. F. Liu, X. Li, L. Lin, Z. B. Yan, S. Dong and J.-M. Liu, Experimental observation of ferroelectricity in multiferroic  $\text{DyMn}_2\text{O}_5$ , *Sci. Rep.* **4**, 3984 (2014).
- <sup>35</sup>G. R. Blake, L. C. Chapon, P. G. Radaelli, S. Park, N. Hur, S.-W. Cheong and J. Rodríguez-Carvajal, Spin structure and magnetic frustration in multiferroic  $\text{RMn}_2\text{O}_5$  ( $\text{R}=\text{Tb}, \text{Ho}, \text{Dy}$ ), *Phys. Rev. B* **71**, 214402 (2005).
- <sup>36</sup>C. R. de la Cruz, B. Lorenz, Y. Y. Sun, C. W. Chu, S. Park and S. W. Cheong, Magnetoelastic effects and the magnetic phase diagram of multiferroic  $\text{DyMn}_2\text{O}_5$ , *Phys. Rev. B* **74**, 180402 (2006).
- <sup>37</sup>H. Kimura, S. Kobayashi, Y. Fukuda, T. Osawa, Y. Kamada, Y. Noda, I. Kagomiya and K. Kohn, Spiral spin structure in the commensurate magnetic phase of multiferroic  $\text{RMn}_2\text{O}_5$ , *J. Phys. Soc. Jpn.* **76**, 074706 (2007).
- <sup>38</sup>R. A. Ewings, A. T. Boothroyd, D. F. McMorro, D. Mannix, H. C. Walker and B. M. R. Wanklyn, X-ray resonant diffraction study of multiferroic  $\text{DyMn}_2\text{O}_5$ , *Phys. Rev. B* **77**, 104415 (2008).
- <sup>39</sup>P. G. Radaelli and L. C. Chapon, A neutron diffraction study of  $\text{RMn}_2\text{O}_5$  multiferroics, *J. Phys.: Condens. Matter* **20**, 434213 (2008).
- <sup>40</sup>G. E. Johnstone, R. A. Ewings, R. D. Johnson, C. Mazzoli, H. C. Walker and A. T. Boothroyd, Magnetic structure of  $\text{DyMn}_2\text{O}_5$  determined by resonant x-ray scattering, *Phys. Rev. B* **85**, 224403 (2012).
- <sup>41</sup>D. Higashiyama, S. Miyasaka, N. Kida, T. Arima and Y. Tokura, Control of the ferroelectric properties of  $\text{DyMn}_2\text{O}_5$  by magnetic fields, *Phys. Rev. B* **70**, 174405 (2004).
- <sup>42</sup>W. Ratcliff, II, V. Kiryukhin, M. Kenzelmann, S.-H. Lee, R. Erwin, J. Schefer, N. Hur, S. Park and S. W. Cheong, Magnetic phase diagram of the colossal magnetoelectric  $\text{DyMn}_2\text{O}_5$ , *Phys. Rev. B* **72**, 060407 (2005).
- <sup>43</sup>S. Kobayashi, T. Osawa, H. Kimura, Y. Noda, I. Kagomiya and K. Kohn, 2D-to-1D modulated-to-lock in successive magnetic phase transitions associated with ferroelectricity in  $\text{ErMn}_2\text{O}_5$ , *J. Phys. Soc. Jpn.* **73**, 1031 (2004).
- <sup>44</sup>S. Kobayashi, T. Osawa, H. Kimura, Y. Noda, N. Kasahara, S. Mitsuda and K. Kohn, Neutron diffraction study of successive magnetic phase transitions in ferroelectric  $\text{TbMn}_2\text{O}_5$ , *J. Phys. Soc. Jpn.* **73**, 3439 (2004).
- <sup>45</sup>S. Kobayashi, H. Kimura, Y. Noda and K. Kohn, Neutron diffraction study of magnetic ordering associated with ferroelectricity in  $\text{TmMn}_2\text{O}_5$ , *J. Phys. Soc. Jpn.* **74**, 468 (2005).
- <sup>46</sup>C. Vecchini, L. C. Chapon, P. J. Brown, T. Chatterji, S. Park, S.-W. Cheong and P. G. Radaelli, Commensurate magnetic structures of  $\text{RMn}_2\text{O}_5$  ( $\text{R}=\text{Y}, \text{Ho}, \text{Bi}$ ) determined by single-crystal neutron diffraction, *Phys. Rev. B* **77**, 134434 (2008).
- <sup>47</sup>G. Beutier, A. Bombardi, C. Vecchini, P. G. Radaelli, S. Park, S.-W. Cheong and L. C. Chapon, Commensurate phase of multiferroic  $\text{HoMn}_2\text{O}_5$  studied by x-ray magnetic scattering, *Phys. Rev. B* **77**, 172408 (2008).
- <sup>48</sup>N. Lee, C. Vecchini, Y. J. Choi, L. C. Chapon, A. Bombardi, P. G. Radaelli and S. W. Cheong, Giant tunability of ferroelectric polarization in  $\text{GdMn}_2\text{O}_5$ , *Phys. Rev. Lett.* **110**, 137203 (2013).
- <sup>49</sup>Z. Y. Zhao, M. F. Liu, X. Li, J. X. Wang, Z. B. Yan, K. F. Wang and J.-M. Liu, Reversing ferroelectric polarization in multiferroic  $\text{DyMn}_2\text{O}_5$  by nonmagnetic Al substitution of Mn, *J. Appl. Phys.* **116**, 054104 (2014).
- <sup>50</sup>Z. Y. Zhao, Y. L. Wang, L. Lin, M. F. Liu, X. Li, Z. B. Yan and J.-M. Liu, Manipulation of Dy-Mn coupling and ferroelectric phase diagram of  $\text{DyMn}_2\text{O}_5$ : The effect of Y substitution of Dy, to be published.
- <sup>51</sup>J. H. Kim, S. H. Lee, S. I. Park, M. Kenzelmann, A. B. Harris, J. Schefer, J. H. Chung, C. F. Majkrzak, M. Takeda, S. Wakimoto, S. Y. Park, S. W. Cheong, M. Matsuda, H. Kimura, Y. Noda and K. Kakurai, Spiral spin structures and origin of the magnetoelectric coupling in  $\text{YMn}_2\text{O}_5$ , *Phys. Rev. B* **78**, 245115 (2008).
- <sup>52</sup>S. Kobayashi, T. Osawa, H. Kimura, Y. Noda, I. Kagomiya and K. Kohn, Reinvestigation of simultaneous magnetic and

- ferroelectric phase transitions in  $\text{YMn}_2\text{O}_5$ , *J. Phys. Soc. Jpn.* **73**, 1593 (2004).
- <sup>53</sup>L. C. Chapon, G. R. Blake, M. J. Gutmann, S. Park, N. Hur, P. G. Radaelli and S. W. Cheong, Structural anomalies and multiferroic behavior in magnetically frustrated  $\text{TbMn}_2\text{O}_5$ , *Phys. Rev. Lett.* **93**, 177402 (2004).
- <sup>54</sup>L. C. Chapon, P. G. Radaelli, G. R. Blake, S. Park and S. W. Cheong, Ferroelectricity induced by acentric spin-density waves in  $\text{YMn}_2\text{O}_5$ , *Phys. Rev. Lett.* **96**, 097601 (2006).
- <sup>55</sup>H. Kimura, Y. Kamada, Y. Noda, K. Kaneko, N. Metoki and K. Kohn, Ferroelectricity induced by incommensurate-commensurate magnetic phase transition in multiferroic  $\text{HoMn}_2\text{O}_5$ , *J. Phys. Soc. Jpn.* **75**, 113701 (2006).
- <sup>56</sup>M. Fukunaga, K. Nishihata, H. Kimura, Y. Noda and K. Kohn, Simultaneous measurements of magnetic neutron diffraction, electrical polarization and permittivity of Multiferroic  $\text{ErMn}_2\text{O}_5$ , *J. Phys. Soc. Jpn.* **76**, 074710 (2007).
- <sup>57</sup>P. G. Radaelli, L. C. Chapon, A. Daoud-Aladine, C. Vecchini, P. J. Brown, T. Chatterji, S. Park and S.-W. Cheong, Electric field switching of antiferromagnetic domains in  $\text{YMn}_2\text{O}_5$ : A probe of the multiferroic mechanism, *Phys. Rev. Lett.* **101**, 067205 (2008).
- <sup>58</sup>M. Fukunaga, Y. Sakamoto, H. Kimura, Y. Noda, N. Abe, K. Taniguchi, T. Arima, S. Wakimoto, M. Takeda, K. Kakurai and K. Kohn, Magnetic-field-induced polarization flop in multiferroic  $\text{TmMn}_2\text{O}_5$ , *Phys. Rev. Lett.* **103**, 077204 (2009).
- <sup>59</sup>P. G. Radaelli, C. Vecchini, L. C. Chapon, P. J. Brown, S. Park and S.-W. Cheong, Incommensurate magnetic structure of  $\text{YMn}_2\text{O}_5$ : A stringent test of the multiferroic mechanism, *Phys. Rev. B* **79**, 020404 (2009).
- <sup>60</sup>M. Fukunaga and Y. Noda, Measurement of complicated temperature-dependent polarization of multiferroic  $\text{RMn}_2\text{O}_5$ , *J. Phys.: Conf. Series* **320**, 012090 (2011).
- <sup>61</sup>J.-H. Kim, M. A. van der Vegte, A. Scaramucci, S. Artyukhin, J.-H. Chung, S. Park, S. W. Cheong, M. Mostovoy and S.-H. Lee, Magnetic excitations in the low-temperature ferroelectric phase of multiferroic  $\text{YMn}_2\text{O}_5$  using inelastic neutron scattering, *Phys. Rev. Lett.* **107**, 097401 (2011).
- <sup>62</sup>C. Wilkinson, P. J. Brown and T. Chatterji, Temperature evolution of the magnetic structure of  $\text{TbMn}_2\text{O}_5$ , *Phys. Rev. B* **84**, 224422 (2011).
- <sup>63</sup>N. Leo, D. Meier, R. V. Pisarev, N. Lee, S.-W. Cheong and M. Fiebig, Independent ferroelectric contributions and rare-earth-induced polarization reversal in multiferroic  $\text{TbMn}_2\text{O}_5$ , *Phys. Rev. B* **85**, 094408 (2012).
- <sup>64</sup>H. Kimura, Y. Sakamoto, M. Fukunaga, H. Hiraka and Y. Noda, Control of magnetic interaction and ferroelectricity by nonmagnetic Ga substitution in multiferroic  $\text{YMn}_2\text{O}_5$ , *Phys. Rev. B* **87**, 104414 (2013).
- <sup>65</sup>A. B. Harris, M. Kenzelmann, A. Aharony and O. Entin-Wohlman, Effect of inversion symmetry on the incommensurate order in multiferroic  $\text{RMn}_2\text{O}_5$  (R=rare earth), *Phys. Rev. B* **78**, 014407 (2008).
- <sup>66</sup>A. B. Harris, A. Aharony and O. Entin-Wohlman, Order parameters and phase diagram of multiferroic  $\text{RMn}_2\text{O}_5$ , *Phys. Rev. Lett.* **100**, 217202 (2008).
- <sup>67</sup>S. Baidya, P. Sanyal, H. Das, B. Roessli, T. Chatterji and T. Saha-Dasgupta, Understanding neutron scattering data in  $\text{YMn}_2\text{O}_5$ : An effective spin Hamiltonian, *Phys. Rev. B* **84**, 054444 (2011).
- <sup>68</sup>D. Higashiyama, S. Miyasaka and Y. Tokura, Magnetic-field-induced polarization and depolarization in  $\text{HoMn}_2\text{O}_5$  and  $\text{ErMn}_2\text{O}_5$ , *Phys. Rev. B* **72**, 064421 (2005).
- <sup>69</sup>G. Giovannetti and J. van den Brink, Electronic correlations decimate the ferroelectric polarization of multiferroic  $\text{HoMn}_2\text{O}_5$ , *Phys. Rev. Lett.* **100**, 227603 (2008).
- <sup>70</sup>S. Dong, J.-M. Liu and E. Dagotto,  $\text{BaFe}_2\text{Se}_3$ : A high  $T_C$  magnetic multiferroic with large ferroelectric polarization, *Phys. Rev. Lett.* **113**, 187204 (2014).
- <sup>71</sup>V. Baledent, S. Chattopadhyay, P. Fertey, M. B. Lepetit, M. Greenblatt, B. Wanklyn, F. O. Saouma, J. I. Jang, and P. Foury-Leykian, Evidence for room temperature electric polarization in  $\text{RMn}_2\text{O}_5$  multiferroics, *Phys. Rev. Lett.* **114**, 117601 (2015).